

Square cylinder in the interface of two different-velocity streams

R. EL MANSY¹, W. SARWAR², J. M. BERGADA¹,
F. MELLIBOVSKY²

¹Fluid Mechanics Department, Universitat Politècnica de Catalunya, 08034, Barcelona, Spain

² Department of Physics, Aerospace Engineering Division, Universitat Politècnica de Catalunya, 08034, Barcelona, Spain

(Received February 3, 2022)

We investigate the incompressible flow past a square cylinder immersed in the wake of an upstream nearby splitter plate separating two streams of different velocity. The bottom stream Reynolds number, based on the square side, $Re_B = 56$ is kept constant while the top-to-bottom Reynolds numbers ratio $R \equiv Re_T/Re_B$ is increased in the range $R \in [1, 6.5]$, corresponding to a coupled variation of the bulk Reynolds number $Re \equiv (Re_T + Re_B)/2 \in [56, 210]$ and an *equivalent* nondimensional shear parameter $K \equiv 2(R-1)/(R+1) \in [0, 1.4667]$. The onset of vortex-shedding, at $R = 2.1 \pm 0.1$ (corresponding to $Re = 86.8 \pm 2.8$, $K = 0.71 \pm 0.04$), is pushed to higher Re as compared to the square cylinder in the classic configuration. The advent of three-dimensionality is triggered by a mode-C-type instability at $R \simeq 3.1$ ($Re \simeq 115$, $K \simeq 1.02$) with wavelength $\lambda_z \simeq 2.4$, much as reported for open circular rings and square cylinders placed at an incidence. The resulting solution is period-doubled and exhibits a triad of spanwise symmetries: a mirror reflection and two spatiotemporal symmetries involving the evolution by half a period (two vortex-shedding cycles) followed by either specular reflection or a half-wavelength shift. The path towards spatio-temporal chaos is initiated thereafter with a modulational period-doubling tertiary bifurcation at $R \in (3.4, 3.8)$ that also doubles the spanwise periodicity. The ensuing nonlinear solution repeats only after four vortex shedding periods and retains only a spatiotemporal invariance consisting in the evolution by half a period (two vortex-shedding cycles) followed by mirror reflection about a streamwise-cross-stream plane. At slightly higher values of $R \geq 4$, the flow has become spatio-temporally chaotic, but the main features of mode C are still clearly distinguishable.

1. Introduction

The flow past circular cylinders has been extensively studied as a paradigm of bluff body aerodynamics (Williamson 1996c), for it involves several interesting phenomena which include, but are not limited to, laminar and turbulent boundary layer separation, vortex shedding, or detached shear layer and wake instabilities. Flow unsteadiness, spatio-temporal chaos and turbulence are a source of aerodynamic noise and vortex-induced vibration, and crucially affect aerodynamic forces, to name but a few issues that are relevant from the engineering applications viewpoint. The sole governing parameter, the Reynolds number, is defined as $Re = UD/\nu$, where U is the free-stream velocity, D the cylinder diameter and ν the kinematic viscosity of the fluid.

Square (Duraó, Heitor & Pereira 1988; Lyn, Einav, Rodi & Park 1995; Luo, Chew & Ng 2003) and rectangular (Okajima 1982; Norberg 1993) cylinders have also been used, albeit to a lesser extent, as an archetype for bluff body aerodynamics. The same definition as for the circular cylinder is used for the Reynolds number, except that D is taken to be the square cylinder side length (or the cross-stream side length for a rectangle).

In real-world applications, bluff bodies are often submerged in boundary layers or wakes and the flow past them is decisively modified by the inhomogeneous velocity profiles of the incoming upstream flow. This is the case of a bridge pillar that is close to the river shore, long-span bridges immersed in an atmospheric boundary layer, underwater pipes near the seabed or subject to strong currents, or a building (or motor vehicle) in the wake of an upstream building (vehicle).

The simplest model for such a situation is the uniform planar shear flow past a circular (Kiya, Tamura & Arie 1980; Tamura, Kiya & Arie 1980; Kwon, Sung & Hyun 1992) or square (Ayukawa, Ochi, Kawahara & Hirao 1993; Hwang & Sue 1997) cylinder, where the homogeneous incoming

streamwise velocity is replaced with a linear profile (constant cross-stream gradient of streamwise velocity and, therefore, constant non-null shear). The shear parameter is defined as $K \equiv DG/U_c$, with D the cylinder characteristic length (diameter and side for circular and square cylinders, respectively), and U_c and $G = (\partial u / \partial y)_{y=y_c}$ the upstream streamwise velocity and dimensional cross-stream gradient of streamwise velocity, respectively, at cylinder mid-height.

Ocasionalmente, the body of interest lies in the way of a thin shear layer rather than a smooth shear profile. This happens, for example, in the near wake of lift-producing devices such as airfoils, stator vanes or rotor blades of compressor and turbines or fans. Struts or rods supporting a structural casing are examples of objects subject to this type of incoming flows. This is precisely the kind of situations we intend to model here by placing a bluff body, the square cylinder, in the interface of two streams with different velocity. The wake-body interaction problem usually considers a body, streamlined or bluff, placed in the wake of another bluff body. The configuration in which a bluff body is placed in the wake of a streamlined body such as we intend to address here has very seldom been considered in the literature, and then always placing a cylinder or strut in the wake of an airfoil (Zhang, Huang & Zhou 2005; Niu, Li & Wang 2021). However distant this problem may seem at first from that of homogeneous upstream shear, the effects associated to the different velocity *seen* by the upper and lower sides of the bluff body might be expected -and will indeed be shown- to bear striking resemblance.

The symmetric and steady flow past a circular cylinder undergoes a supercritical Hopf bifurcation, the primary instability, at around $Re^H \simeq 47$ with frequency $St^H \simeq 0.12$ (Provansal *et al.* 1987; Norberg 1994), resulting in a time-periodic two-dimensional solution that consists in the alternated shedding of opposite-signed vortices from either side of the cylinder – a flow configuration commonly referred to as Kármán vortex street (von Kármán 1911, 1912). Although the spatial Z_2 symmetry associated to vertical reflection about a diametral plane aligned with the incoming flow is broken (Marques *et al.* 2004), a spatio-temporal Z_2 symmetry persists in the form of flow invariance upon the combined effect of evolution by a half period followed by reflection about the same original reflection-symmetry plane.

The periodic and space-time-symmetric two-dimensional vortex-shedding solution might be observed in experiments all the way up to $Re \lesssim 190$, three-dimensionality consistently arising from this point on (Williamson 1996a). Two distinct three-dimensional vortex-shedding modes have been reported in the so-called wake transition regime, whose inception results in two corresponding discontinuities of the Strouhal number (St) dependence on Re (Williamson 1988). The first one, mode A, is characterised by the onset of vortex loops that are stretched by shear into streamwise vortex pairs of spanwise wavelength around $3 \sim 4D$ and has been shown to persist at flow regimes as low as $Re \gtrsim 180$, thus coexisting with the two-dimensional solution over a small range of Reynolds numbers (Williamson 1996b). Mode A is only regularly patterned at the early stages of inception and then only transiently, but soon after develops intermittent large-scale spot-like wave dislocations that render the spanwise structure rather irregular (Williamson 1992). The second, mode B, arises at slightly higher values of the Reynolds number $Re \gtrsim 250$ and exhibits a fairly regular spanwise pattern with a shorter characteristic wavelength of about $\sim 1D$ (Williamson 1996b). Mode-B-type vortical structures pervade the near wake even at flow regimes where turbulence has already set in at much higher Reynolds numbers in excess of 1000 (Mansy *et al.* 1994). Floquet stability analysis has shown that mode A emanates from a secondary instability of the two-dimensional periodic vortex-shedding solution at $Re^A = 188.5 \pm 1$ with wavelength $\lambda_z^A = 3.96 \pm 0.02$, and happens to be subcritical (Henderson & Barkley 1996), hence the hysteretical flow behaviour. Meanwhile, mode B seems to be related to a second instability of the same solution that occurs supercritically at $Re = 259 \pm 2$ with $\lambda_z^B = 0.822 \pm 0.007$ (Barkley & Henderson 1996). The critical values of the parameters at bifurcation have since been further refined to $(Re^A, \lambda_z^A) = (190.2 \pm 0.02, 3.966 \pm 0.002)$ and $(Re^B, \lambda_z^B) = (261.0 \pm 0.2, 0.825 \pm 0.002)$ using asymptotically large domains (Posdziech & Grundmann 2001). A third mode, consisting of a complex-conjugate pair of eigenvalues and dubbed QP on account of its introducing quasi-periodicity into the flow, has been identified as dominant at intermediate wavelengths of about $\sim 2D$, in between those characterising modes A and B (Blackburn & Lopez 2003). Mode QP bifurcates at $Re^{QP} \simeq 377$ and generates branches of unstable, and therefore not experimentally realisable, quasi-periodic states (Blackburn *et al.* 2005).

The spatio-temporal Z_2 symmetry of the two-dimensional vortex-shedding regime coexists with

the spanwise invariance of the infinite-cylinder flow problem, represented by the orthogonal group $O(2)=Z_2 \times SO(2)$, which includes reflection about any discretionary plane that is orthogonal to the spanwise direction (Z_2) and every arbitrary translation along the span ($SO(2)$). Systems with $Z_2 \times O(2)$ symmetry, where the Z_2 refers to a spatio-temporal symmetry, rather than simply spatial, and $O(2)$ to space invariance, admit two types of synchronous codimension-one bifurcations, one preserving the space-time Z_2 symmetry and the other one breaking it (Marques et al. 2004). Two-dimensional time-periodic vortex-shedding past a circular cylinder belongs to this symmetry class and, among the secondary instabilities that three-dimensionalise the flow, mode A is triggered by a Z_2 -preserving bifurcation, while mode B is induced by one that breaks it (Blackburn et al. 2005). Whenever the bifurcation in a system with the aforementioned symmetries involves a complex-conjugate pair that is non-resonant with the destabilising two-dimensional time-periodic and space-time symmetric solution, three quasi-periodic solution branches arise, namely a pair of symmetry-conjugate modulated travelling waves and a third of modulated standing waves. Only one of the two distinct types of solution branches -either the pair of travelling or the standing waves- might be stable at a time (Marques et al. 2004). The third three-dimensionalising secondary instability of the two-dimensional time-periodic wake past a circular cylinder corresponds precisely to a quasi-resonant quasi-periodic subcritical bifurcation. The two symmetry-conjugate branches of modulated travelling-wave solutions add an unstable eigenmode to the count of the already unstable two-dimensional solution, while the modulated standing wave adds two (Blackburn et al. 2005). The neighbouring 1:4 resonant case, which would correspond to a period-doubling bifurcation, is a codimension-two bifurcation and would therefore require the tuning of a second parameter beside the Reynolds number for a complete unfolding. The symmetry group of the two-dimensional vortex-shedding regime admits also a number of mixed-mode bifurcations and strong 1:1 and 1:2 resonances, all codimension-two, none of which seems to bear any relevance to the cylinder wake problem (Marques et al. 2004).

Square-cylinder wake dynamics bears compelling resemblance to that past a circular cylinder. The symmetries of the problem are the same and the primary instability leads to a two-dimensional time-periodic and space-time symmetric vortex-shedding state at the slightly lower $Re^H \simeq 45$ and $St^H \simeq 0.10$ (Norberg 1996; Park & Yang 2016). There are however notable differences that concern the location where the boundary layer separates from the cylinder surface. While separation points can migrate freely on the surface of a circular cylinder, they are bound to coincide with the corners of a square or rectangular cylinder. As it happens, separation occurs from the rear corners only at very low Reynolds number, and then only after reattachment from an initial separation from the front corners (Okajima 1982; Robichaux et al. 1999; Yoon et al. 2010).

The flow past a square cylinder also exhibits mode A- and B-type structures in the wake transition regime (Sohankar et al. 1999; Saha et al. 2003; Luo et al. 2003; Bai & Alam 2018), but their respective occurrence starts at lower values of the Reynolds number $Re^A \simeq 160 \pm 2$ and $Re^B \simeq 204 \pm 5$ and present somewhat larger wavelengths $\lambda_z^A/D \simeq 5.1 \pm 0.1$ and $\lambda_z^B/D \simeq 1.3 \pm 0.1$ at onset (Luo et al. 2007). While early experiments failed to detect any hysteresis in the inception of mode A and no discontinuity in the Strouhal number dependence on Reynolds number was observed (Luo et al. 2003), later experiments that strived to accurately resolve variations in the driving parameter produced a small hysteretical region (Luo et al. 2007; Tong et al. 2008).

Linear instabilities akin to modes A and B of the flow past a circular cylinder have been identified through Floquet stability analysis also in the wake transition regime of the flow past a square cylinder (Robichaux et al. 1999), alongside a third, subharmonic, quasi-periodic mode. As for the circular cylinder, modes A and B preserve and break, respectively, the spatio-temporal Z_2 symmetry of the two-dimensional vortex-shedding solution, but occur at lower $Re^A \simeq 164$ and $Re^B \simeq 197$, with slightly longer $\lambda_z^A/D \simeq 5.2$ and $\lambda_z^B/D \simeq 1.1$ at bifurcation (Sheard et al. 2009; Choi et al. 2012). Modulated travelling- and standing-wave solution branches also arise in the wake of a square cylinder following the bifurcation of a complex-conjugate pair (Blackburn & Lopez 2003), which is the counterpart to quasi-periodic mode QP of the circular cylinder. Mode QP, which bifurcates at $Re^{QP} \simeq 215$ with $\lambda_z \simeq 2.6$ for the square cylinder (Sheard et al. 2009), was originally mistaken for a subharmonic (period-doubling) bifurcation on account of its being of a quasi-resonant quasi-periodic type, and following a shortcoming of the stability analysis method used in finding what they called mode S (Robichaux et al. 1999). Unlike what happens for the flow past a circular

cylinder, the symmetry-conjugate branches of modulated travelling-wave solutions issued from the QP bifurcation are supercritical and inherit the stability properties of the two-dimensional solution, while the modulated standing-wave branch, which is also supercritical but with a lesser slope at bifurcation, adds an unstable eigenmode (Blackburn *et al.* 2005).

Nonlinear analysis using the Landau equation as a model for the secondary instability of the flow past a square cylinder points to a supercritical nature of mode A at bifurcation (Sheard *et al.* 2009), as opposed to what happens for the circular cylinder (Henderson & Barkley 1996), and in overt contradiction with experimental observation (Luo *et al.* 2007). This dispute as to the subcritical or supercritical nature of mode A between numerical simulation and experiment has not yet been settled to the authors knowledge.

The relation between the instabilities (both primary and secondary) in the wake of square and circular cylinders has recently been elucidated by the numerical smooth transformation of the former into the latter by gradual rounding of the corners (Park & Yang 2016). The primary Hopf bifurcation that brings about two-dimensional vortex shedding is initially slightly delayed as the cylinder geometry evolves from circular to square, but the trend is reversed halfway and the critical value brought down to $Re^H \simeq 44.7$. The bifurcation remains supercritical all along. Secondary three-dimensionalising instabilities also evolve continuously and uneventfully, gradually advancing the occurrence of the bifurcations of all three-modes, A, B and QP, to lower critical values of Re . The order of bifurcation is not altered, but the bifurcation points get closely packed, with mode QP strongly promoted for the square in comparison to the circular shape. Meanwhile, the wavelength at criticality is slightly but steadily increased for all three modes in the morphing from circular to square.

The top-bottom Z_2 reflection symmetry of the flow past an infinitely long cylinder might be broken in several possible ways. For a circular cylinder, the symmetry disruption might be achieved by introducing curvature along the spanwise direction turning the cylinder into a ring (Monson 1983; Leweke & Provansal 1994, 1995; Sheard *et al.* 2003), by applying rotation about its centerline (Kang *et al.* 1999; Mittal & Kumar 2003), by subjecting it to a non-uniform upstream velocity profile (incoming shear flow) (Jordan & Fromm 1972; Kiya *et al.* 1980; Tamura *et al.* 1980; Park & Yang 2018), or by combining incoming shear with rotation (Yoshino & Hayashi 1984; Sung *et al.* 1995), among other options. Upstream shear is also an option for breaking the symmetry of the square cylinder problem (Hwang & Sue 1997; Saha *et al.* 1999; Sohankar *et al.* 2020), as also is placing the cylinder at an incidence with respect to the incoming flow (Norberg 1993; Sohankar *et al.* 1998; Tong *et al.* 2008; Yoon *et al.* 2010), or combining both effects together. In most cases, the two-dimensional time-periodic vortex-shedding solution persists upon deliberately breaking the spatial Z_2 symmetry of the problem, but the space-time Z_2 symmetry is no longer fulfilled (Blackburn & Sheard 2010).

The primary instability of the flow past an open ring leads to an axisymmetric time-periodic vortex-shedding regime (Monson 1983; Leweke & Provansal 1994), analogous to the two-dimensional vortex-shedding regime past a circular cylinder but obviously lacking its spatio-temporal Z_2 symmetry. Numerical studies have shown that, besides the instabilities related to the classic modes A and B, a subharmonic mode C also emerges and is the dominant secondary instability for rings of aspect ratio around $\Gamma \equiv d/D = 5$, defined as the quotient between the diameter of the circle described by the cylinder axis (d) and the cylinder diameter itself (D) (Sheard *et al.* 2003). Both experiments and direct numerical simulation show that the secondary linear instability develops nonlinearly into a period-doubled vortex-shedding solution with a distinct wavelength somewhere in between those predicted by Floquet stability analysis for modes A and B in the ring wake (Sheard *et al.* 2005a,b). Although the solution is period-doubled, aggregate quantities such as aerodynamic forces preserve the original period. Two instants exactly one shedding cycle apart are mutually related by an appropriate symmetry operation (any of either a spanwise/azimuthal rotation by half the angular wavelength or reflection about some collection of appropriately chosen diametral planes) and the period-doubling does not initiate a period-doubling cascade. Instead, the mode-C structures that characterise the wake after the secondary bifurcation are replaced by mode-A-type structures when the Reynolds number is further increased. The scenario that follows seems to be analogous to that for the circular cylinder

A subharmonic instability analogous to mode C is also dominant for a square cylinder placed

at moderate incidence angles α (Sheard et al. 2009). Mode A, which was originally believed to be dominant for all incidences following experiments that unfortunately failed to check the flow topology at intermediate values of α (Tong et al. 2008), is in fact overtaken by mode C for $\alpha \gtrsim 10.5^\circ$ (Yoon et al. 2010; Sheard 2011), which is in turn outdone by another mode of characteristics similar to those of mode A for $\alpha \gtrsim 26^\circ$. This second mode A' is distinct from the one evolving from $\alpha = 0^\circ$ in that it evolves from the space-time symmetric mode A corresponding to $\alpha = 45^\circ$. Numerical evidence seems to discard any smooth connection between modes A and A' by mere continuous tilting of the cylinder from one incidence to the other, although the physical flow mechanisms at play appear to be the same. Mode-B-type structures have also been detected in experiments above a critical Reynolds number that also evolves smoothly as the incidence angle is changed across the full range (Tong et al. 2008). The presence of mode-B structures in the tilted cylinder wake has been confirmed by direct numerical simulation at sufficiently high values of the Reynolds number (Sheard et al. 2009), which in this case is usually defined with the cross-stream projected height $D \times (\cos \alpha + \sin \alpha)$ instead of just D .

Mode QP of the flow past circular and square cylinders is only the third linear instability, after modes A and B, of the periodic and space-time symmetric two-dimensional vortex-shedding solution, and the associated growth rate is much smaller. It is therefore not to be expected that wake structures related to mode QP might be observed in actual experiments. It does however bear strong resemblance to the mode C observed in the wake behind open rings (Sheard et al. 2005a) of the right moderate aspect ratio and square cylinders at intermediate incidence angles (Sheard et al. 2009), regarding both spanwise wavelength and flow topology. As a matter of course, a weak disruption of the spatial Z_2 symmetry in problems belonging to the $Z_2 \times O(2)$ symmetry group will alter the nature and characteristics of the secondary bifurcations. Modes A and B may preserve their respective symmetries only approximately, but the incommensurate frequencies of mode QP, which did not retain any remnant of the spatio-temporal Z_2 symmetry, might experience a locking into some strong resonance. As it happens, mode QP is quasi-resonant for both circular and square cylinder flows and, as the span is curved into a ring or the square tilted into incidence, the associated complex-conjugate pair of Floquet multipliers approaches the negative real axis, collides, and separates into a couple of negative real eigenvalues, *i.e.* two subharmonic/period-doubling modes (Blackburn & Sheard 2010; Sheard 2011). It is thus that mode QP evolves into mode C, which eventually overtakes modes A and B in driving the secondary instability once the reflection symmetry across the midplane has been sufficiently broken.

Upstream shear has been shown in experiments to delay the onset of periodic vortex shedding, *i.e.* Re^H increases with K , to the point that shedding can be completely suppressed all the way up to $Re < 220$ (Kiya et al. 1980). This effect has also been observed in numerical simulation (Tamura et al. 1980). Other computational studies, however, did not detect the phenomenon despite exploring similar values of the parameters (Lei et al. 2000; Cao et al. 2010).

Stability analysis seems to favour the notion that Re^H is mostly unaffected by K , and that, if anything, it is marginally promoted to slightly lower values, from 46.5 for $K = 0$ to 45.5 for $K = 0.2$ (Park & Yang 2018). Floquet stability analysis shows that the wake transition regime is instead greatly affected by upstream shear. While modes A, B and QP bifurcate at successively large values ($Re^A \simeq 190$) < ($Re^B \simeq 250$) < ($Re^{QP} \simeq 380$) in the symmetric problem, mode QP locks into subharmonic mode C as K is increased and gradually overtakes mode B and mode A for $K = 0.1$ and 0.2 , respectively (Park & Yang 2018). As a matter of fact, modes A and B are pushed to higher $Re^A \simeq 240$ and $Re^B \simeq 300$, while mode C is advanced to as low as $Re^C \simeq 150$ for $K = 0.2$. While the critical spanwise wavelength of mode A slightly increases to $\lambda_z^A \simeq 4.2$, mode B remains mostly unaltered at $\lambda_z^B \simeq 0.8$ and mode C somewhat narrows to $\lambda_z^C \simeq 1.6$ for $K = 0.2$. Numerical simulation has seen mode-A-type structures suppressed, and with them three-dimensionality, at $Re \simeq 200$ with $K \gtrsim 0.1$, accompanied by the ensuing discontinuity in the St vs Re relationship (Cao et al. 2010). This phenomenon has not been observed in experiments and the emergence of longitudinal vortical structures in the upstream flow may be accounted responsible.

The onset of time-dependence Re^H is slightly advanced and the mean drag coefficient C_d and Strouhal number St reduced for the flow past a square cylinder subjected to increasing K (Cheng et al. 2007; Lankadasu & Vengadesan 2008). At these very low values of Re , C_l is negative and its

modulus increases with increasing K (Cheng et al. 2007; Lankadasu & Vengadesan 2008), but the trend is reversed at higher Re (Lankadasu & Vengadesan 2011).

The decrease in Re^H has been belied by 2D simulations that explored larger values of K and reported suppression of two-dimensional vortex shedding behind a square cylinder at sufficiently low values of $Re \lesssim 200$ whenever $K \gtrsim K_c$ exceeds a certain critical value that increases with Re (Ray & Kumar 2017; Cheng et al. 2007). As for the circular cylinder, an increasing K renders top vortices stronger and rounder, while bottom vortices become weaker and elongated and dissipate fast in the wake (Ray & Kumar 2017). As for the circular cylinder, the stagnation point systematically rises above the cylinder midplane upon increasing K at any value of Re (Cao et al. 2014).

In the presence of upstream shear, the wake behind a square cylinder experiences a unique secondary three-dimensionalising instability characterised by a single mode (Lankadasu & Vengadesan 2011), instead of the two modes A and B that are sequentially observed in the wake transition regime for both circular and square cylinders in the absence of upstream shear. This single mode, which arises at $Re \simeq 140 \sim 150$ when $K = 0.2$, was initially mistaken for mode B (Lankadasu & Vengadesan 2011) because of its similar wavelength, but the solution seems in fact period-doubled. Its three-dimensional structure appears shifted by half a wavelength after every vortex-shedding cycle, so that the instability would plausibly correspond to mode C, which would have taken precedence over modes A and B following the disruption of the spatial Z_2 symmetry. At $Re = 200$ and $K = 0.2$, three-dimensional simulations have shown mode-A- and mode-B- type structures on the low- and high-velocity halves, respectively, of the wake (Lankadasu & Vengadesan 2009), although nothing similar has been reported elsewhere.

Here we choose to submerge the square cylinder in a thin shear layer by replacing the classic upstream homogeneous shear by a piecewise-constant velocity profile with the discontinuity separating the top and bottom homogeneous streamwise velocities precisely located at cylinder mid-height. This same setup has been used twice before, but the flow was expressly kept two-dimensional (Mushyam & Bergada 2017; An et al. 2020). In order to simulate experimentally reproducible conditions, we choose to separate the top and bottom homogeneous velocity streams by a flat plate, such that the shear layer results from the reunion, at its trailing edge, of the top and bottom boundary layers and develops smoothly downstream before reaching the cylinder. This kind of upstream conditions may be obtained experimentally in a wind or water tunnel (Loucks & Wallace 2012), and the development of the shear layers thus generated have been thoroughly investigated (Rogers & Moser 1992; Moser & Rogers 1993). The length of the plate, the gap left between its trailing edge and the cylinder and the Reynolds number below the plate are kept constant. The top-to-bottom stream velocity ratio $R \equiv U_T/U_B$ has been varied and the various distinct flow topologies that arise classified. The onset and evolution of three-dimensional structures in the cylinder wake are analysed and discussed in detail.

The paper is structured as follows. The mathematical modelling is presented in section §2 alongside the numerical approach undertaken. §3 dissects the flow generated by the interaction of the two different-velocity streams as they flow parallel in the splitter plate wake towards the square cylinder. A temporal characterisation of the resulting flow past the cylinder is then given in section §4, followed by an analysis of aerodynamic performances trends in section §5. Finally, the wake transition regime is dissected in section §6 and the main results summarised and conclusions drawn in section §7.

2. Mathematical modelling and numerical approach

Figure 1 presents the side and front views of the computational domain employed in the simulations. The square cylinder, of side D , is located at the origin of the domain, of size $L_x \times L_y = 34.5D \times 16D$, at a distance $L_x^u = 9D$ downstream from the domain inlet, and at mid-height, such that the top and bottom boundaries are at a distance $L_y/2 = 8D$ above and below the centreline (blockage ratio $B = 0.0625$). All cases were studied with incidence $\alpha = 0^\circ$ (all sides are either parallel or orthogonal to the incoming flow direction). The splitter plate, of chord $L = 6.5D$ and negligible thickness, extends horizontally from domain inlet at mid-height, thus leaving a $2D$ gap between its trailing edge and the front face of the cylinder. The small distance left for the development of the shear layer has been checked to be sufficiently short to keep it thin and stable while at the same time long enough for the flow to freely adapt to the presence of the cylinder (see section

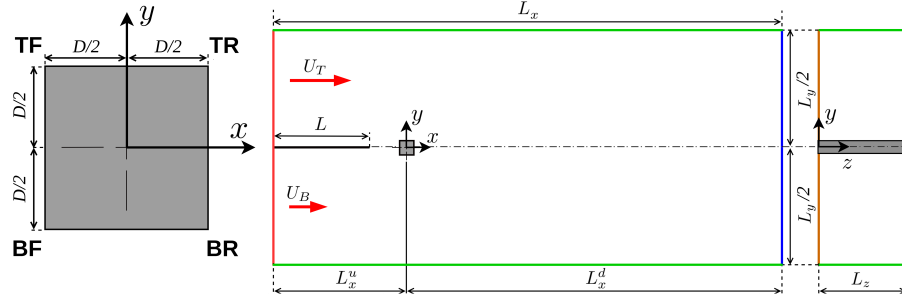


Figure 1: Computational domain. The square cylinder, of side D , is located at midheight of the domain, of height L_y , at distances L_x^u and L_x^d from the upstream and downstream boundaries, respectively. The cylinder is placed at zero angle of attack and the origin is set at its centre. The flat plate, of negligible thickness and chord L , is also at mid-height, horizontal, and starts at the upstream boundary. For three-dimensional simulations the domain is periodic in the spanwise direction with length L_z . The colours indicate the boundary condition types: velocity inlet (red, with velocities U_T and U_B for the top and bottom streams, respectively), pressure outlet (blue), slip walls (green), non-slip walls (black) and periodic (orange).

3). Meanwhile, the short splitter plate helps smooth the initiation of the shear layer while keeping the boundary layer thin and laminar. A downstream extent of $L_x^d = L_x - L_x^u = 25.5D$ has been allowed to properly capture the wake and avoid interferences of the domain outlet with the flow around the cylinder and in its near-wake.

The Navier-Stokes equations for incompressible flow, nondimensionalised with the square cylinder side length D and the mean upstream flow velocity $U = (U_T + U_B)/2$ (U_T and U_B are the top and bottom stream constant velocities), read

$$\begin{aligned} \frac{\partial \mathbf{u}}{\partial t} + (\mathbf{u} \cdot \nabla) \mathbf{u} &= -\nabla p + \frac{1}{Re} \nabla^2 \mathbf{u}, \\ \nabla \cdot \mathbf{u} &= 0, \end{aligned} \quad (2.1)$$

where $\mathbf{u}(\mathbf{r}; t) = (u, v, w)$ and $p(\mathbf{r}; t)$ are the nondimensional velocity and pressure, respectively, at nondimensional location $\mathbf{r} = (x, y, z)$ and advective time t (units of D/U). Here, x (u), y (v), and z (w) denote the streamwise, crossflow, and spanwise coordinates (velocity components), respectively.

Neumann boundary conditions for pressure ($\nabla p \cdot \hat{\mathbf{n}} = 0$) and Dirichlet for velocity have been prescribed at domain inlet. The velocity profile has been taken as a piecewise-constant function, with $\mathbf{u} = U_B \hat{\mathbf{i}} = 2U/(R+1) \hat{\mathbf{i}}$ below the splitter plate and $\mathbf{u} = U_T \hat{\mathbf{i}} = 2UR/(R+1) \hat{\mathbf{i}}$ above it. No-slip boundary conditions have been enforced on cylinder walls and splitter plate ($\mathbf{u} = 0$, $\nabla p \cdot \hat{\mathbf{n}} = 0$). The top and bottom domain boundaries have been taken as slip walls with $\mathbf{u} \cdot \hat{\mathbf{n}} = 0$ and $[(\nabla \mathbf{u}) \cdot \hat{\mathbf{n}}] \times \hat{\mathbf{n}} = \mathbf{0}$, and the domain outlet has been set as homogeneous Dirichlet ($p = 0$) for pressure and homogeneous Neumann ($\nabla \mathbf{u} \cdot \hat{\mathbf{n}} = \mathbf{0}$) for velocity. Periodic boundary conditions in the spanwise direction have been prescribed for three-dimensional simulations.

The two governing parameters are the Reynolds number and the top-to-bottom stream velocity ratio

$$Re \equiv \frac{UD}{\nu}, \quad R \equiv \frac{U_T}{U_B},$$

where ν is the kinematic viscosity of the fluid.

Two separate Reynolds numbers might be defined individually for the top and bottom streams as

$$Re_T \equiv \frac{U_T D}{\nu} = \frac{2R}{1+R} Re \quad \text{and} \quad Re_B \equiv \frac{U_B D}{\nu} = \frac{2}{1+R} Re,$$

and used as an alternative set of governing parameters.

For the somewhat-related problem of a bluff body immersed in upstream shear, the shear parameter is usually defined by nondimensionalising the free-stream velocity gradient as

$$K \equiv \frac{D}{U} \left(\frac{\partial U}{\partial y} \right)_{\infty}$$

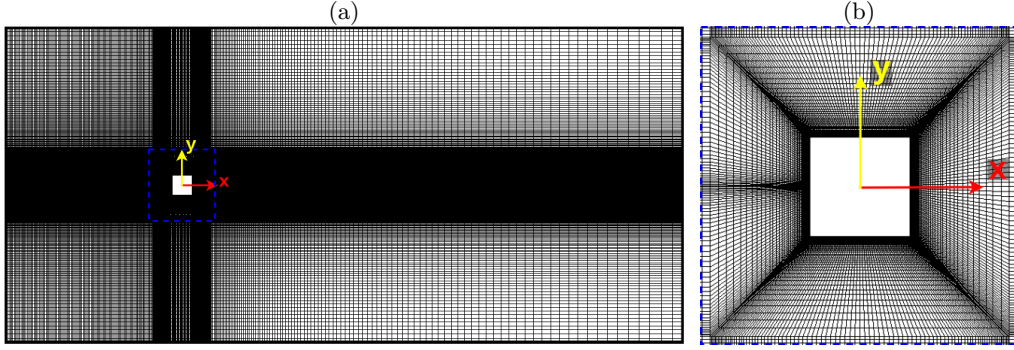


Figure 2: Computational mesh. (a) Full domain and (b) detail around the square cylinder.

Here the free stream velocity is a step function and an equivalent shear parameter can be defined with the average free-stream velocity gradient over the characteristic length of the cylinder as $K \equiv 2(R - 1)/(R + 1)$.

As we will see in §3, the incoming-flow shear profile is anything but homogeneous, but a parallel can still be drawn on account of the mean shear effects over the cylinder characteristic length, even if shear is concentrated within a thinner layer. This would indicate that part of the phenomenology observed in the presence of homogeneous upstream shear is in fact related to the velocity difference/jump perceived locally by the upper and lower sides of the body under scrutiny, rather than the global effect of the velocity gradient alone.

The bottom stream Reynolds number has been kept fixed to $Re_B = 56$ throughout the study, while the top-to-bottom stream velocity ratio has been varied in the range $R \in [1, 5.375]$. A $\Delta R = 0.2$ step has been used to resolve $R \in [1, 3]$ while higher velocity ratios have been tested at a set of discrete values $R \in \{3.1, 3.2, 3.3, 3.4, 3.8, 4, 5.375\}$. The equivalent Reynolds number and shear parameter, which are linked to R , have been simultaneously varied in the ranges $Re \in [56, 178]$ and $K \in [0, 1.37]$.

Wall shear (τ_w) and pressure (p) have been non-dimensionalised into the friction and pressure coefficients as

$$C_f \equiv \frac{\tau_w}{\frac{1}{2}\rho U^2} \quad \text{and} \quad C_p \equiv \frac{p - p_\infty}{\frac{1}{2}\rho U^2}, \quad (2.2)$$

with p_∞ the far field pressure, while their added integral over the cylinder surface, the aerodynamic force, has been projected into the classical lift (F_l) and drag (F_d) components per unit length and non-dimensionalised into the lift and drag force coefficients following

$$C_l \equiv \frac{F_l}{\frac{1}{2}\rho D U^2} \quad \text{and} \quad C_d \equiv \frac{F_d}{\frac{1}{2}\rho D U^2}. \quad (2.3)$$

The incompressible Navier-Stokes equations have been evolved in time using Nektar++, an opensource code based on the spectral/hp element method framework (Cantwell et al. 2015). This method combines the geometric flexibility of the finite element method with the high-order accuracy of spectral methods. We have employed the velocity correction scheme, which is made to be consistent with its overall temporal accuracy by an appropriate high-order discretisation of the pressure on all boundaries (Cantwell et al. 2015; Moxey et al. 2020).

The in-plane two-dimensional structured mesh, consisting exclusively of quad elements, is shown in figure 2. A particularly high resolution has been employed on all no-slip wall surfaces to properly resolve boundary layers, as well as along the splitter plate and cylinder wakes. Away from these regions, the mesh density has been allowed to relax. Tensor-products of Lagrange polynomial bases of order 6 have been deployed within each quadrilateral element and spanwise Fourier expansions have been used in the homogenous spanwise direction for three-dimensional computations. Polynomial expansions of orders 4 to 8 were initially tested for the highest velocity ratio, but 6 was chosen for the exploration as it provided a fair compromise between accuracy and computational burden.

An in-plane mesh consisting of $N_{xy} = 95294$ 6th-order quadrilateral elements has been used for all simulations with velocity ratios in the range $R \in [1, 3.4]$, with the time step gradually reducing

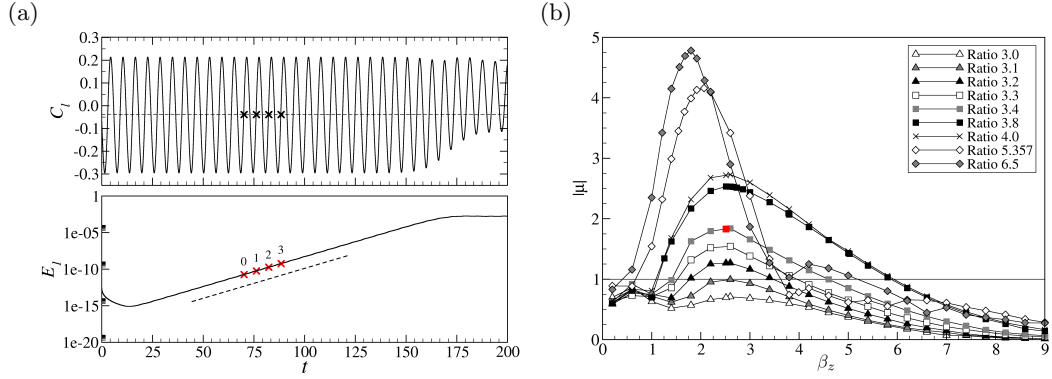


Figure 3: Stability analysis of the flow past a square cylinder in the interface of two different-velocity streams with $Re_B = 56$. (a) Time-evolution of the lift coefficient C_l (top) and of the modal energy associated to the only spanwise-dependent Fourier mode E_1 considered (bottom) for $(R, \lambda_z) = (3.4, 2.5)$. The red crosses indicate $\{C_l = \langle C_l \rangle_t; \dot{C}_l > 0\}$ Poincaré crossings in the linear regime used for the exponential fit (red dashed line). (b) Least stable Floquet multipliers for velocity ratios in the range $R \in [3, 6.5]$. The red square corresponds to the case analysed in panel (a).

from $\Delta t = 0.0028$ to 0.0012 . A second finer mesh with $N_{xy} = 125204$ 6th-order quad elements has been employed for $R > 3.4$ and the time step reduced from $\Delta t = 0.0007$ at $R = 3.8$ to $\Delta t = 0.0004$ at the highest $R = 5.357$. A thorough code validation alongside a resolution study is presented in A.

The requirements for the spanwise size of the computational domain at any given value of the Reynolds number and velocity ratio can be assessed by determining the range of wavenumbers that are unstable. This can be done with a full-fledged Floquet analysis, but given that only the dominant eignmode for each spanwise wavenumber, rather than the full spectrum (or even a subset of it), is actually required, the stability analysis has been carried out by simply time-stepping on a quasi 3D domain, adding to the two-dimensional field a unique spanwise Fourier mode of the chosen wavelength, randomly initialised to a very low energy level (See appendix B).

Figure 3a illustrates the time-stepping-based stability analysis for $(R, \lambda_z) = (3.4, 2.5)$. After some initial transients, the energy associated to the only spanwise mode considered ($E_1(t)$, bottom) starts growing exponentially, with a barely perceptible superimposed oscillation that is inherited from the underlying two-dimensional vortex-shedding periodicity (C_l , top). An exponential fit (dashed line) to the Poincaré crossings in the linear growth regime (red crosses) provides an estimation of the modulus of the unstable multiplier $|\mu|$.

The results of the stability analysis for varying R and λ_z are presented in figure 3b. The actual onset of flow three-dimensionality occurs for $R \simeq 3.1$. Below this value, all three-dimensional perturbations decay (the Floquet multiplier has $|\mu| < 1$) and the flow remains two-dimensional. The largest modulus Floquet multiplier corresponds to a fairly constant spanwise wavenumber of about $\lambda_z = 2\pi/\beta_z \simeq 2.4$ all the way up to $R \leq 4$ and then steadily increases to 2.8 for $R = 6.5$. Consequently, a spanwise domain size $L_z = 2.5$ (and integer multiples of it) constitutes a fair choice if the fastest-growing three-dimensional mode is to be represented in the simulation. The smooth evolution of the spectrum indicates that, despite its evolution in wavelength, the same mode is responsible for the instability over the whole range of R explored. At $R = 6.5$, however, a second unstable mode, of much shorter associated wavelength $\lambda_z \simeq 1.5$ has destabilised. The first mode is clearly dominant, but the presence of this second mode may play some role in shaping the small-scale vortical structures that are present in the wake once fully developed turbulence has kicked in.

In accordance with the Floquet stability analysis, spanwise lengths $L_z = 5$ have been employed in most three-dimensional computations, deploying resolutions in the range $N_z \in [28, 40]$ to guarantee six orders of magnitude energy decay in the spanwise Fourier spectrum. A few cases with $L_z = 10$ and $N_z = 80$ have been run at the highest explored values of R to confirm that the observed solution features are not an artifact of overly limited domain size.

R	Mesh	L_z	N_{xy}	N_z	$N = N_{xy} \times N_z$	L_z/N_z	Δt
1	Mesh B	-	95294	-	-	-	0.0028
\vdots							\vdots
3.1	Mesh B	-	95294	-	-	-	0.0014
3.4	Mesh B	5	95294	28	2.668×10^6	0.179	0.0012
3.8	Mesh C	5	125204	34	4.256×10^6	0.147	0.0007
4.0	Mesh C	5	125204	36	4.507×10^6	0.138	0.0006
5.357	Mesh C	10	125204	80	10.016×10^6	0.125	0.0004

Table 1: Summary of the space and time discretisations used in the present computations.

Table 1 summarises the space and time discretisations used for the several computations run in the present study.

For completeness, the code and mesh validation are presented in full in appendix A.

3. Incoming upstream flow

The initially flat interface of two parallel viscous streams flowing at different speeds is not stable. The step profile of purely streamwise velocity at best diffuses into an increasingly wide shear layer or, more generally, destabilises following a Kelvin-Helmholtz instability. The aim here is to subject the square cylinder to as close a step profile as experimentally feasible by keeping the distance over which the two streams interact to a minimum while still allowing the upstream flow to adapt to the incoming obstacle. In order to smooth the development of the shear layer, the two streams have been allowed to flow over a flat plate for some distance before meeting, sufficiently long for a Blasius boundary layer to develop but at the same time short enough for it to remain thin and laminar.

Figure 4 depicts cross-stream profiles of streamwise velocity as the flow develops over the splitter plate and downstream along its wake, which constitutes a shear layer for $R > 1$. The flow is essentially two-dimensional and steady in this region for all cases considered, but spanwise and time averaging has been applied nonetheless.

In the absence of the square cylinder (dashed lines), laminar boundary layers of the Blasius type naturally develop on both surfaces of the splitter plate. For $R = 1$ (light gray) top and bottom boundary layers are symmetric and generate a top-down symmetric velocity profile in the wake that diffuses gradually as the centre-line velocity, which coincides with the streamline issued from the trailing edge of the flat plate, progressively recovers. The asymmetry is already evident for $R = 2$ (dark gray) and becomes increasingly marked for $R = 3.4$ (red) and 5.357 (green), but the centreline velocity defect is recovered all the same as the velocity profile adopts a smoothed step-like shape that connects the top- and bottom-stream velocities fairly linearly over about half the square cylinder height by the time the flow reaches the (absent) cylinder location. The higher the value of R , the faster and greater the velocity defect recovery with respect to the slow stream, such that the negative shear associated to the lower side of the shear layer becomes barely detectable. The resulting region of roughly homogeneous shear is noticeably shifted towards the high velocity side. Meanwhile, the trailing-edge streamline remains horizontal independently of R , as ascertained by the zero cross-stream velocity distribution along the wake centre line in the inset of figure 4. None of the cases run for the splitter plate alone resulted in any instability of its wake or trailing shear layer, such that the flow fields remained two-dimensional and steady.

We will be placing the square cylinder at a downstream distance from the splitter plate trailing edge where the unperturbed flow is characterised by a parallel profile of purely streamwise velocity that is neither linear nor a step function, but can be assimilated to a step function smoothed over about half the cylinder height. Anyhow, whatever the profile looks like across the cylinder height, it can be considered as fairly flat above and below the cross-stream locations where the top and bottom surface of the cylinder will be, with respective velocities those of the fast and slow streams.

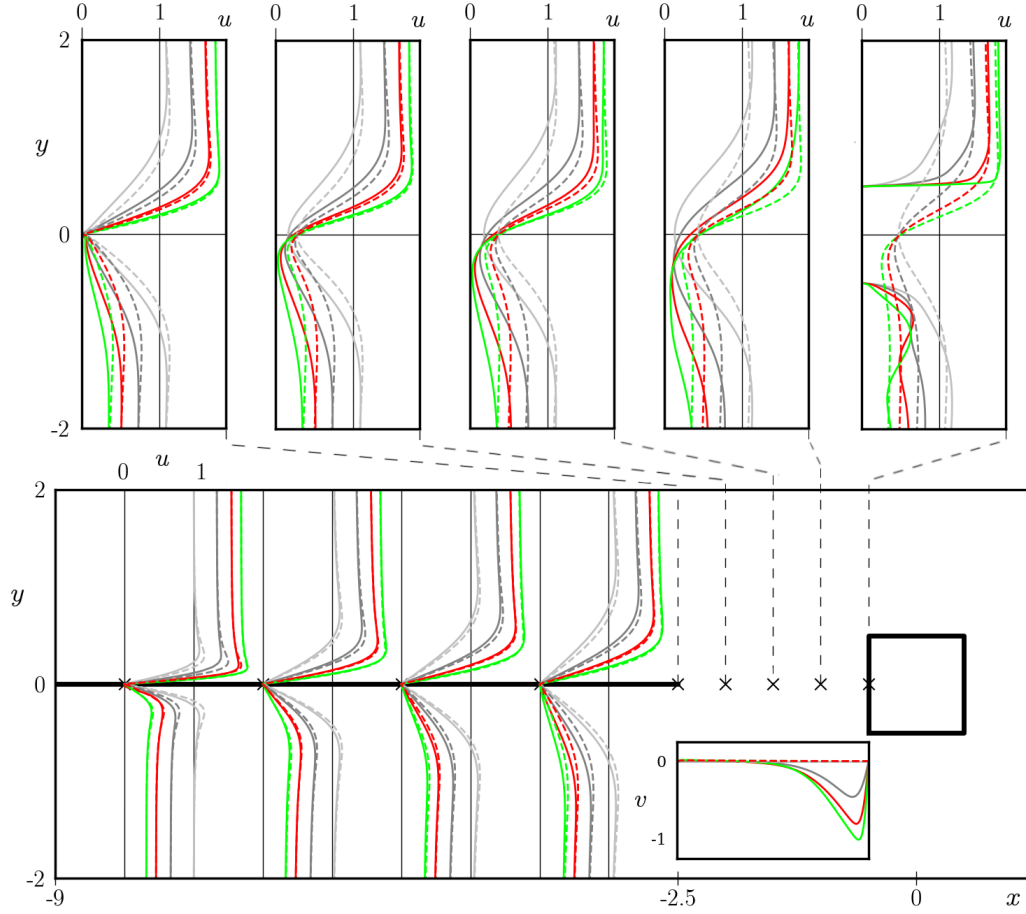


Figure 4: Span- and time-averaged characterisation of the incoming flow as it develops on the splitter plate and downstream along the near wake, covering the gap with the square cylinder. Shown are Cross-stream profiles of streamwise velocity over the flat plate (main panel) the plate-cylinder gap (top panels), along with centre-line distribution of cross-stream velocity in the gap (inset). Velocity ratios $R = 1$ (light gray), 2 (dark gray), 3.4 (red), and 5.357 (green) have been represented both in the presence (solid) and absence (dashed) of the cylinder.

The streamwise velocity can therefore be taken as approximating to some extent the intended step profile.

The presence of the cylinder (solid lines), introduces a blockage that obviously affects the incoming flow. The boundary layers on the top and bottom surfaces of the flat plate are somewhat thickened, particularly on the low velocity side and for low values of R , albeit only slightly. The massflow blockage becomes all the more prominent as we dive into the plate wake. The shear layer remains fairly thin while the presence of the cylinder is still not decisively felt, but the streamwise velocity recovery along the wake is hindered and the lowest velocity is shifted towards the slow stream as R is increased. The thickening of the shear layer as the cylinder is approached and its downwards bias results in something like a (not-quite) homogeneous shear profile that spreads over the cylinder height, but still flattens to about constant velocity above and below the cylinder. In addition, a net downwards cross-stream velocity builds up along the wake that transfers massflow from the high velocity stream to the low velocity stream. An increasingly larger portion of the fast stream flies below the cylinder as the velocity ratio is increased.

4. Temporal characterisation of the flow

The starting case $(Re_B, R) = (56, 1)$, which roughly corresponds to the homogeneous flow past a square cylinder at $Re = 56$, is steady and reflection symmetric with respect to the horizontal mid-

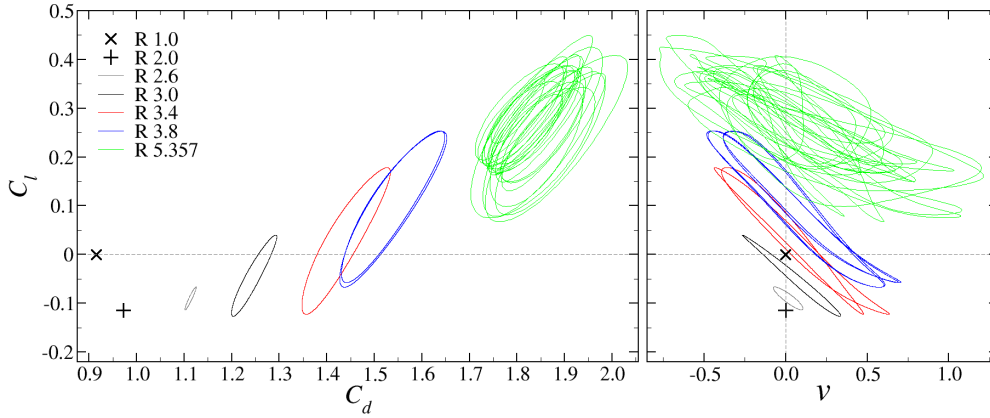


Figure 5: Phase maps projections on the (C_l, C_d) and (C_l, v) , with v the cross-stream velocity at $(x, y, z) = (2, 0, z_m)$, where z_m has been chosen in each case to pick the largest amplitude in the evolution of v for consistency.

plane ($y = 0$). The presence of the splitter plate reduces the effective incoming velocity through viscous effects and, consequently, has a stabilising effect on the flow past the square cylinder, which is otherwise expected to display periodic vortex-shedding already at this Re (Norberg 1996). The flow remains steady but the symmetry is broken as the velocity ratio is increased at constant $Re_B = 56$ all the way up to $R \leq 2$. This is illustrated by the point phase-map projections for $R = 1$ (cross) and $R = 2$ (plus sign) in figure 5. The symmetric case $R = 1$ is characterised by $C_l = v = 0$, while $R = 2$ has evidently lost the symmetry (also $v \neq 0$, but small enough to be imperceptible to the naked eye). Soon after, a Hopf bifurcation somewhere in the range $R^H \in (2, 2.2)$ introduces time-dependence, such that solutions are characterised by asymmetric time-periodic vortex shedding. The periodicity shows up in the phase-map projections of figure 5 as closed loops, and the oscillation amplitude grows fast as R is increased. The onset of time dependence occurs for a bulk Reynolds number and shear parameter $(Re^H, K^H) \simeq (87 \pm 3, 0.71 \pm 0.04)$, way larger than the critical threshold for the square cylinder in homogeneous flow, which undergoes a Hopf bifurcation at $Re^H \simeq 45 \sim 53$ (Kelkar & Patankar 1992; Sohankar et al. 1998; Lankadasu & Vengadesan 2008). The critical threshold found here corresponds to fairly high K and moderately low Re , which is consistent with previous observation that vortex-shedding might be suppressed/delayed by upstream shear (Cheng et al. 2007; Ray & Kumar 2017). Upstream shear has therefore a stabilising effect, as previously reported also for the circular cylinder (Kiya et al. 1980; Tamura et al. 1980), although some studies attest to the contrary both for circular (Park & Yang 2018) and square cylinders (Lankadasu & Vengadesan 2008). Figure 6a shows the spectrum ($|\hat{C}_l|$) of the lift coefficient signal ($C_l(t)$, portrayed in the inset) for $R = 3$ (black line in figure 5). A clear peak is clearly identifiable at $f_1 = 0.155$, along with a few harmonics of decaying amplitude at integer multiples of the main frequency. The solution remains periodic and the fundamental peak and harmonics move to higher f_1 as the velocity ratio is increased to $R = 3.4$ (figure 6b). Besides the slight drift of the Strouhal frequency, an essential alteration has occurred that is not perceptible in the C_l spectrum, nor in the (C_l, C_d) phase-map projection for that matter, but becomes obvious instead from the (C_l, v) phase-map projection (red line in figure 5). The actual period of the solution is not that of the C_l or C_d signals but double, and only shows in time-series of local quantities such as point velocity probe readings. The period doubling is related to the three-dimensionalisation of the flow, which has earlier been shown to occur at $R \simeq 3.1$, corresponding to $(Re, K) \simeq (115, 1.02)$. The spanwise invariance of the two-dimensional vortex-shedding flow is disrupted in a way that preserves a triad of remaining spanwise symmetries (spanwise reflection, half period evolution followed by spanwise reflection and half period evolution followed by half spanwise wavelength shift) that will be discussed later. All three symmetries retain the original period for all variables that aggregate/average over the spanwise direction, as is the case of force coefficients, but the actual invariance after a full vortex-shedding cycle requires the further composition with a space operation

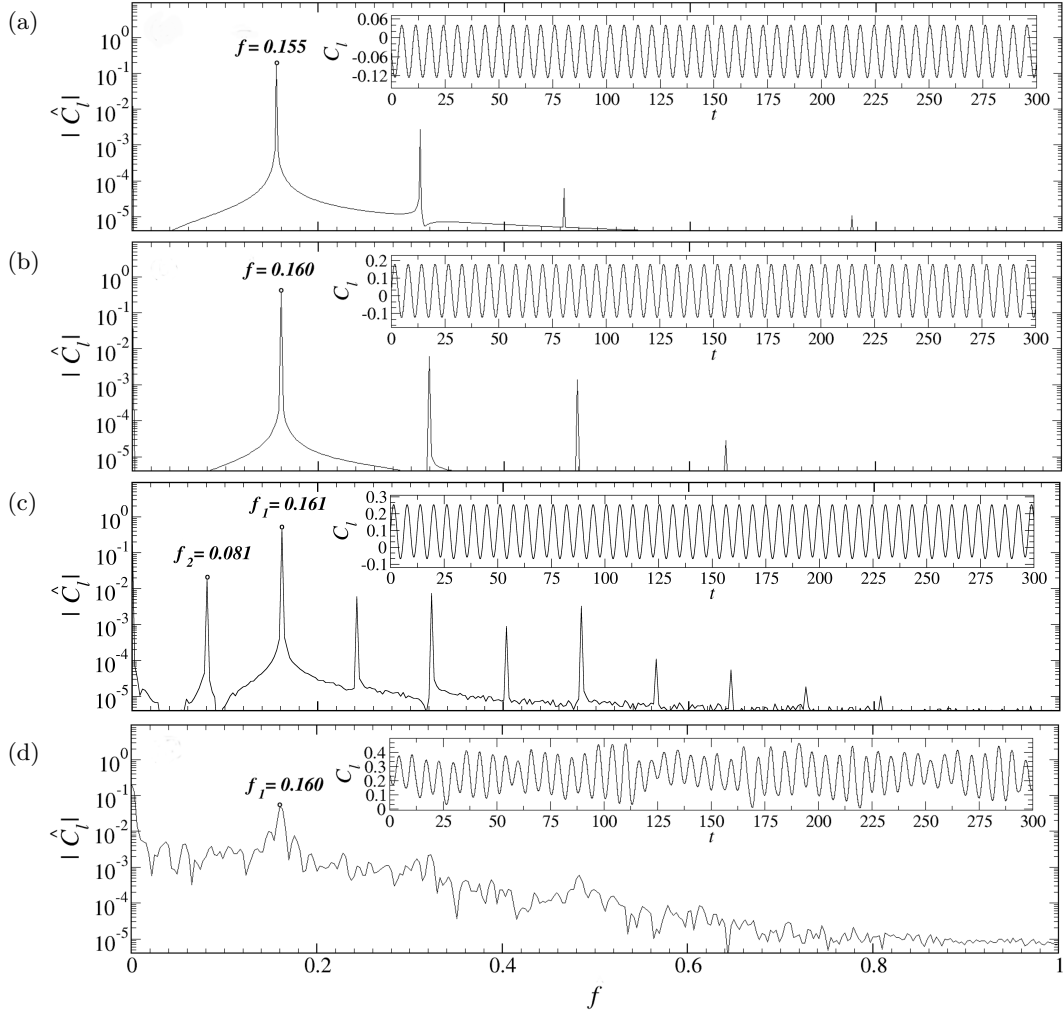


Figure 6: $|\hat{C}_l|$ Power spectra of the lift coefficient for different velocity ratios. The insets shows the time series of drag coefficient versus advective time and the phase diagram for drag and lift coefficients. (a) $R = 3$, (b) $R = 3.4$, (c) $R = 3.8$, (d) $R = 5.357$.

and the original solution is only fully recovered after a second vortex-shedding cycle, which makes the solution qualify as period-doubled.

At $R = 3.8$, a second period doubling of an altogether different nature has occurred. Now the bifurcation affects not only local variables but also aggregates, as clearly shown by the double loop in the (C_l, C_d) and the four-fold loop in the (C_l, v) phase-map projections (blue line in figure 5). As a matter of fact, local variables repeat only after four vortex-shedding cycles. The fundamental peak f_1 in the C_l spectrum is still dominant in figure 6c, but a subharmonic peak at the exact half frequency $f_{1/2} = f_1/2$ has arisen along with its harmonics. The flow topology only repeats every four vortex-shedding cycles, but a space-time symmetry operation still exists that renders the flow invariant after every two vortex-shedding cycles (half a period) provided an appropriate spanwise reflection is also applied.

At $R = 5.357$ the flow has become temporally chaotic (green line in figure 5) and though the main fundamental peak and its first few harmonics are still discernible in the spectrum of figure 6d, they are accompanied by high-energy broadband noise. The second period-doubling bifurcation identified here is suggestive of a period-doubling cascade as the origin of chaotic dynamics, although this cannot be concluded from the rather coarse discretisation of parameter space investigated in the present study.

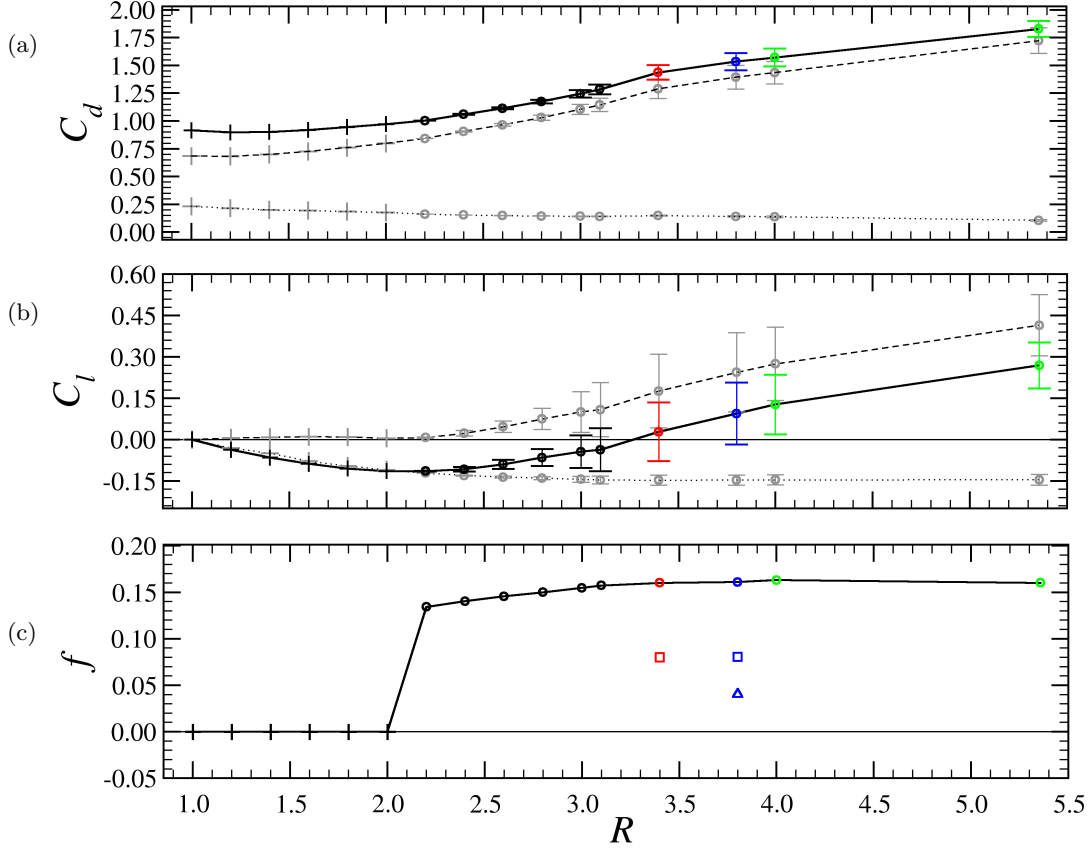


Figure 7: Performance parameters as a function of the velocity ratio R at constant bottom Reynolds number $Re_B = 56$. (a) Drag coefficient C_d . (b) Lift coefficient C_l . (c) Strouhal number f and, for period-doubled solutions, subharmonic frequencies (squares for the half and triangle for the quarter frequency). Different symbols denote steady (plus signs) and unsteady (circles) solutions. Colour coding separates 2D (black), 3D periodic (red), 3D period-doubled (blue) and chaotic (green) solutions. Total force coefficient trends (solid lines) are split into their pressure (dashed) and friction (dotted) components. Error bars denote oscillation amplitude.)

5. Aerodynamic performances

The evolution of the drag (C_d) and lift (C_l) coefficients as the velocity ratio R is increased at a constant bottom Reynolds number $Re_B = 56$ is presented in figures 7a and b, respectively. The oscillation amplitude is indicated by error bars for unsteady regimes, and different symbols and colours denote different types of solutions (plus sign: steady; circle: unsteady; black: 2D periodic; red: 3D periodic; blue: 3D period-doubled; green: chaotic). After a barely perceptible decrease, C_d starts growing steadily as R is increased through the various flow regimes. This dependence is consistent with the combined effect of increasing K , which tends to reduce C_d (Saha et al. 1999; Lei et al. 2000; Cheng et al. 2007), and also increasing Re , which makes it grow fast (Davis & Moore 1982; Franke et al. 1990; Saha et al. 2003; Mahir 2017). The combined effect of both parameters shows that the dependence of C_d on K changes from a declining trend at low $Re \lesssim 100$ to increasing beyond this value (Sohankar et al. 2020). Some simulations, both two- and three-dimensional, at very low $Re < 200$ and $K < 0.5$ predict a decreasing trend of C_d (Cheng et al. 2007) also with Re . The additive decomposition of $C_d = C_d^p + C_d^f$ into its pressure (C_d^p , dashed) and friction (C_d^f , dotted) components, reveals how pressure forces dominate over viscous forces across the full regime, as is typical of bluff body aerodynamics. As a matter of fact, C_d^f declines with R , so that C_d^p takes a larger and larger fraction of the total C_d . For circular cylinders, C_d^p has been shown to take a constant proportion of total C_d independently of K , but this is only valid for constant Re and the trend expected for rising Re is actually increasing (Tamura et al. 1980; Lei et al. 2000). The

initial decline of C_l is much more pronounced and results in a clear downforce as R is increased from symmetric. This follows from the fast drop of C_l^f for low R , with friction downforce taking the lead over pressure lift, which remains negligible while the symmetry disruption is moderately low. The decreasing trend is reversed as the Hopf bifurcation renders the flow time-periodic at $R \in (2, 2.2)$ and C_l^p starts growing fast, but actual positive average lift is not achieved until the flow has become three-dimensional for $R \in (3.1, 3.4)$. Prior to that, positive lift is recovered over some parts of the vortex-shedding cycle, even if on average it remains negative. Once the initial reduction is overcome, the increasing trend is sustained over the full range of R explored because while friction downforce C_l^f saturates, pressure lift C_l^p keeps growing. Net downforce has been reported for the square cylinder in homogenous shear at $Re \leq 100$ and moderate $K \leq 0.5$ (Cheng et al. 2007; Lankadasu & Vengadesan 2008), while positive lift is recovered for $Re \geq 150$ (Lankadasu & Vengadesan 2011; Sohankar et al. 2020), in agreement with present results. As for C_d , the C_l trend with K is a decreasing one for $Re \lesssim 120$ and a growing one above this threshold (Sohankar et al. 2020). The oscillation amplitude increases fast after the initial Hopf bifurcation for both C_d and C_l , as expected from 2D numerical literature results (Sohankar et al. 2020; Saha et al. 1999), but it almost saturates by the time three-dimensionality has kicked in. The escalating fluctuations that follow from increasing Re might be partially or totally compensated by a decline associated to increasing K (Lankadasu & Vengadesan 2011). Most of the force oscillation can be ascribed to pressure fluctuation, as friction behaves rather stably.

The evolution of the Strouhal number (vortex-shedding frequency f) across the full exploration, measured at several locations in the near wake at $(x, y, z) = (2.5, 0, 0)$, $(2.5, 0, 2.5)$ and $(3.5, 0, 0)$, is shown in figure 7c. After the debut of vortex-shedding at the Hopf bifurcation, the frequency drifts to slightly higher values but remains mostly unaltered thereafter. The strouhal number f is expected to grow fast with Re while vortex-shedding remains two-dimensional and to stagnate for a while thereafter across the wake transition regime before starting a slow decline (Okajima 1982; Davis & Moore 1982; Kelkar & Patankar 1992; Norberg 1993; Sohankar et al. 1999; Saha et al. 2003). The trend with K is a slightly decreasing one, at least for sufficiently low $Re < 200$ (Ayukawa et al. 1993; Saha et al. 1999; Cheng et al. 2007; Kumar & Ray 2015), so that it cannot be discarded that the combined effect produces the slowly increasing and then saturating behaviour observed here.

The onset of three-dimensionality, introduces a new frequency (see figure 7c) that is exactly half the Strouhal number (squares), and the ensuing period-doubling adds yet a third quarter-frequency to the solution (triangle).

6. Three-dimensionalisation of the flow: Wake transition regime

The reflection symmetry about the horizontal midplane is broken by setting $R \neq 1$. In these conditions, the only remaining symmetries of the problem concern the spanwise direction. The problem is thus *only* invariant under the orthogonal group $O(2)=SO(2) \times Z_2$ symmetry, involving both arbitrary spanwise shifts ($SO(2)$) and mirror reflections about all planes orthogonal to the spanwise direction (Z_2). As long as the solutions remain two-dimensional, spanwise invariance is preserved, and the onset of time dependence is a matter of no moment.

The bifurcation that triggers three-dimensionality, though, necessarily breaks the translational invariance $SO(2)$ and restricts the mirror symmetry Z_2 to a collection of z -planes equispaced at intervals $\lambda_z/2$, where λ_z is the fundamental spanwise wavelength of the arising three-dimensional solutions. Two-dimensional periodic solutions may still destabilise following both synchronous or quasiperiodic bifurcations, as was the case in the presence of the space-time Z_2 symmetry (Marques et al. 2004; Blackburn et al. 2005), but none of the two possible types of synchronous bifurcations can preserve a symmetry that was not there in the first place. If the quasiperiodic bifurcation becomes resonant and turns into a period-doubling bifurcation, the original time-periodicity is broken but still retained in the form of a space-time symmetry that recovers the solution after evolution over the original period (half the new period) followed by reflection about any z -plane located halfway between consecutive mirror-symmetry planes. In this guise, the period of the three-dimensional solution is double that of the destabilising two-dimensional solution, but shall appear to be the same whenever aggregate quantities are monitored. The phase maps in figure 5 suggest that the advent of three-dimensionality follows precisely this path, as has been shown to occur

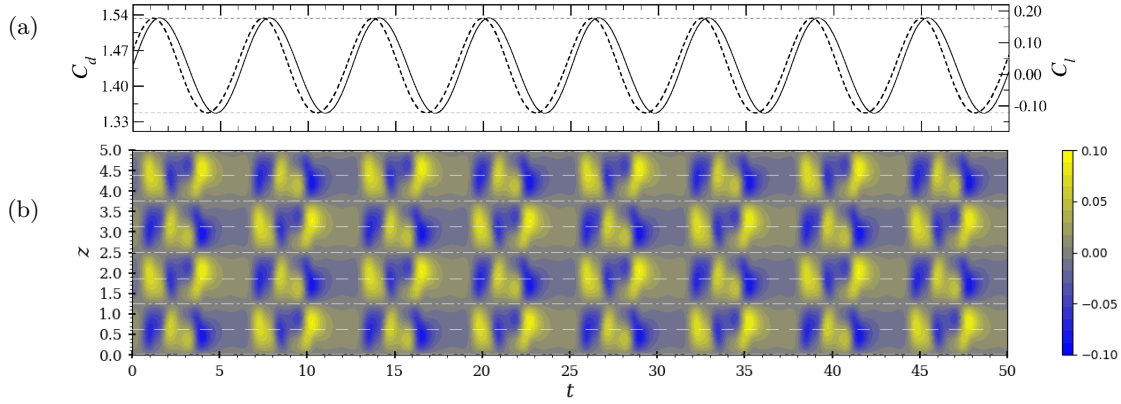


Figure 8: Space-time properties of the $R = 3.4$ solution. (a) Dynamic evolution of the lift C_l (solid) and drag C_d (dashed) coefficients. (b) Space-time diagrams of spanwise velocity $w(x, y, z; t)$ at probe location $(x, y) = (6.0, 0.5)$. Reflection (dash-dotted white lines) and time-shift plus reflection (dashed white) symmetry planes are indicated.

for other systems breaking the space-time symmetry of the two-dimensional solution (Blackburn & Sheard 2010) such as circular rings (Sheard *et al.* 2005b,a) or inclined cylinders (Sheard *et al.* 2009; Sheard 2011).

Figure 8b contains space-time diagrams of spanwise velocity $w(x, y, z; t)$ along a probe array located at $(x, y) = (6.0, 0.5)$ alongside corresponding time series of C_l and C_d (panel a) for the three-dimensional periodic solution at $R = 3.4$. The space-time diagrams correspond to 8 vortex-shedding cycles, as clear from the C_l and C_d time series, and their periodicity corresponds exactly with that of vortex shedding. The space-time diagrams show instead that the actual periodicity of the solution is twice that of vortex shedding, as previously unraveled by the corresponding phase maps in figure 5. The nature of the period doubling, which does not affect aggregate quantities, is now clearly explained as a result of the way in which the spanwise invariance has been disrupted upon three-dimensionalisation of the flow. The reflection Z_2 symmetry is only preserved at all times about planes located at $z = z_0 + (2j)\lambda_z/4$ (white dash-dotted lines), where the origin for the spanwise coordinate has been chosen to enforce $z_0 = 0$, $\lambda_z = 2.5$ here and $j \in \mathbb{Z}$. Additionally, a space-time symmetry operation consisting in the evolution by half a period $T/2$, where T is the actual period of the solution corresponding to two vortex-shedding cycles, followed by reflection about any plane located at $z = z_0 + (2j + 1)\lambda_z/4$ (white dashed lines) also leaves the solution invariant. The appropriate composition of the two symmetries shows that the solution is also invariant to evolutions by half a period $T/2$, followed by a spanwise shift by a half wavelength $\lambda_z/2$.

The ensuing period-doubling bifurcation is of an altogether different nature. The solution at $R = 3.8$ has an actual period of four vortex-shedding cycles, yet aggregate quantities repeat every two vortex-shedding cycles. Close inspection of figure 9a shows how the C_l and C_d time series have a period that is about twice that for $R = 3.4$. The space-time diagram for w provide the full picture. The bifurcation that produces the period-doubled solution is spatially subharmonic in the sense that the spanwise wavelength is double that at $R = 3.4$. It is a modulational instability to perturbations of a wavelength twice that of the bifurcating solution. This breaks the mirror symmetry and the only remaining symmetry leaves the solution invariant to evolution for half a period (two vortex-shedding cycles) followed by reflection about planes located at $z = z_0 + j\lambda_z/2$ (white dashed line), where $\lambda_z = 5$ now.

A three-dimensional representation of the solution at $R = 3.4$ is shown in figure 10a at two consecutive crossings of the Poincaré section defined by $C_l = \langle C_l \rangle_t$ and $\dot{C}_l > 0$. Spanwise mode zero, shown with a transparent iso-surface for $\omega_z = \pm 0.1$, is taken to represent the Kármán vortices. The three-dimensional vortical structures present in the flow are exposed by means of the Q-criterion, which identifies vortical structures as regions where the second invariant of the velocity gradient tensor becomes positive ($Q > 0$), i.e. the rotation rate overcomes the shear rate (Hunt 1988). Streamwise-cross-stream vortical structures are made visible through $Q = 0.0002$ isocon-

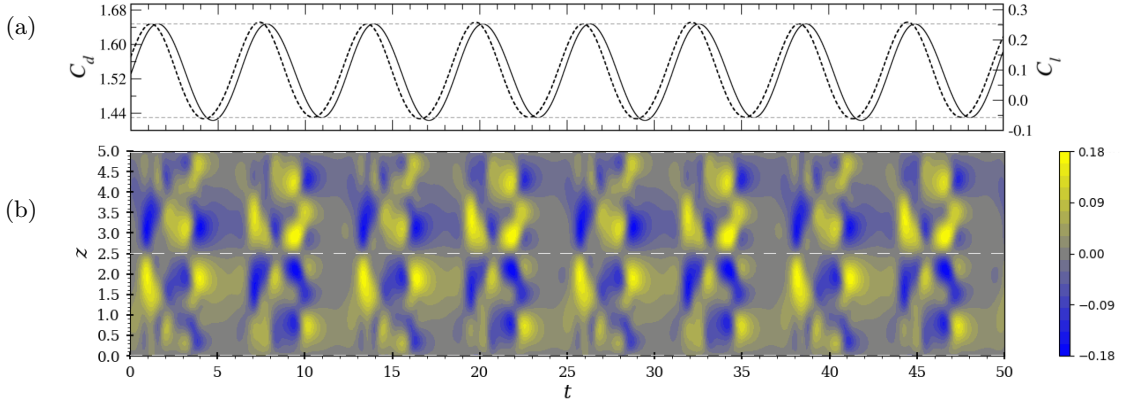


Figure 9: Space-time properties of the $R = 3.8$ solution. (a) Dynamic evolution of the lift C_l (solid) and drag C_d (dashed) coefficients. (b) Space-time diagrams of spanwise velocity $w(x, y, z; t)$ at probe location $(x, y) = (6.0, 0.5)$. Time-shift plus reflection symmetry planes (dashed white) are indicated.

tours coloured by streamwise vorticity ω_x . A first visible effect of three-dimensionalisation is that of introducing spanwise modulation to Kármán vortices, whose vorticity is no longer merely spanwise but has become slightly tilted and alternates positive and negative values of the streamwise component. Elongated streamwise-cross-stream vortices extend along the braids connecting consecutive Kármán vortices. The three-dimensional flow topology is very different from mode-A- and mode-B-type structures observed for circular (Williamson 1996c) and square (Bai & Alam 2018) cylinders in the wake transition regime. Instead, the streamwise-cross-stream vortices, in particular their wavelength and time periodicity, is highly reminiscent of mode QP in the wake of circular (Blackburn et al. 2005), square (Robichaux et al. 1999; Blackburn et al. 2005) and rounded-square (Park & Yang 2016) cylinders, provided that the positive Kármán vortices emanating from the bottom shear layer are overlooked and the elongated vortices in the braids connecting them to the preceding and following negative Kármán vortices duly spliced. As a matter of fact, the parallel is all the more convincing when a comparison is drawn between the present three-dimensional wake vortices and mode C structures in the wake of open rings (Sheard et al. 2005a), squares at incidence (Sheard et al. 2009) or cylinders submerged in upstream shear (Park & Yang 2018).

Comparing two snapshots exactly one Poincaré section crossing apart, the aforementioned space-time symmetries become apparent. The solution looks exactly the same but shifted by exactly half a wavelength in the spanwise direction or reflected about appropriate symmetry planes as previously observed. The fully developed three-dimensional solution bears strong resemblance and shares the same symmetries with the dominant eigenmode of the underlying two-dimensional periodic solution at the same value $R = 3.4$, as clear from figure 10. Here the most unstable mode of figure 3b for $\lambda_z = 2.5$ has been represented using the Q-criterion and coloured by ω_x (symmetric arbitrary range). The unstable two-dimensional solution is indicated by transparent $\omega_z = \pm 0.1$ iso-surfaces that clearly show the Kármán vortices. The topologies of the dominant eigenmode and of the three-dimensional solution are evidently related and so is the space-time symmetry dynamics as illustrated by snapshots taken one Poincaré crossing apart.

The symmetries and wavelength of the dominant eigenmode (and, with it, the nonlinear solution) make it analogous to the mode C that destabilises the axisymmetric/two-dimensional periodic solutions characteristic of the flow past a circular ring (Sheard et al. 2005b,a) or an inclined square cylinder (Sheard et al. 2009; Sheard 2011), which evolve from the respective modes QP of the top-bottom symmetric cases and take precedence over modes A and B when the symmetry has been sufficiently disrupted. Mode C, its evolution from mode QP in a codimension-2 bifurcation, and its overtaking modes A and B, has been recently exposed in the somewhat related case of a circular cylinder in homogeneous upstream shear (Park & Yang 2018). Here we are only varying one parameter R , so that modes A and B are never encountered along the particular $Re - K$ path followed. The rapid increase of the upstream velocity ratio and its associated mean shear is probably suppressing them before any trace can be even found in the Floquet spectrum.

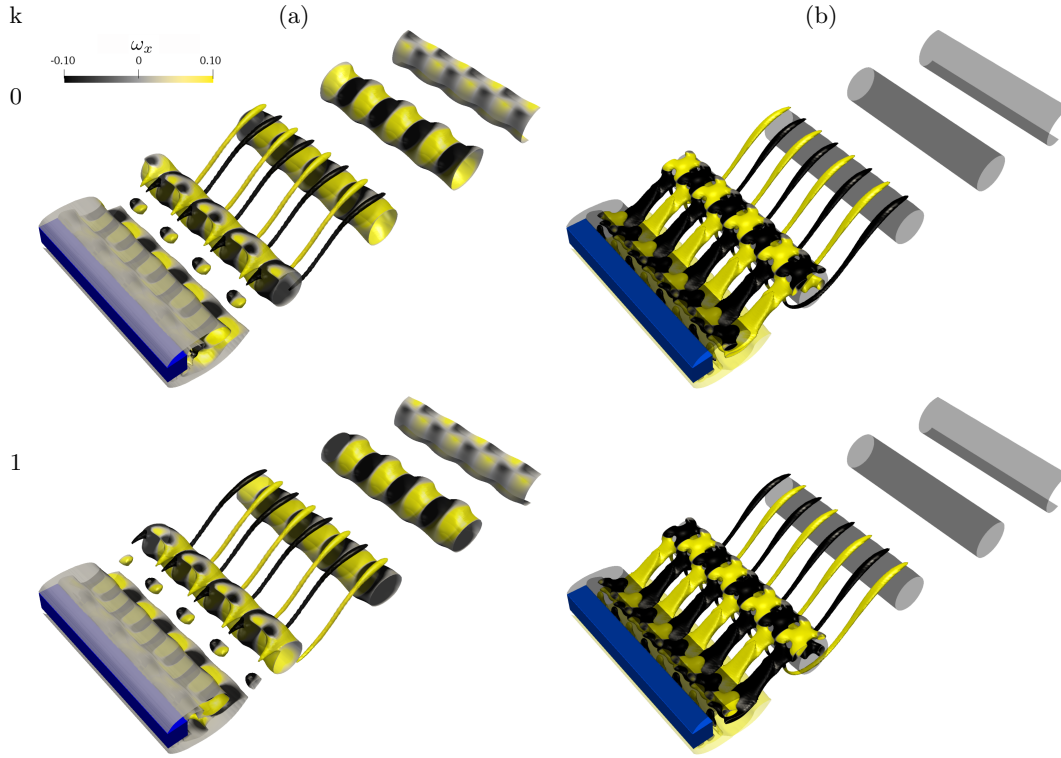


Figure 10: Instantaneous snapshots of (a) the three-dimensional solution at $R = 3.4$ (Movie 1) and (b) corresponding dominant eigenmode of the underlying two-dimensional solution (Movie 2), at two consecutive crossings of the Poincaré section. Shown are iso-surfaces of the Q-criterion ($Q = 0.0002$ for three-dimensional solution, arbitrarily chosen for the dominant eigenmode to ease comparison), coloured by streamwise vorticity (symmetric arbitrary scale for the eigenmode). Spanwise vortices are shown with transparent iso-surface for $\omega_z = \pm 0.1$. The solution is replicated twice in the spanwise direction to $L_z = 10$ only for visualisation purposes.

The dominant eigenmode of the underlying two-dimensional solution is the same for all values of R investigated here. With minor variations, it remains topologically identical from as low as $R = 3$, which corresponds to a stable case, to as high as $R = 6.5$, where the three-dimensional solution has evolved into chaotic dynamics. The most unstable (or least stable) wavelength remains around $\lambda_z \simeq 2.5$ for low values of R and then gradually grows as R is increased. In particular, the most unstable mode remains the same for $R = 3.8$, for which it has been seen that a second bifurcation has taken place and the space-time symmetry of $R = 3.4$ is no longer present. It is to be surmised that the period doubling bifurcation, that appears to arise from a spanwise subharmonic/modulational instability of the $R = 3.4$ solution to perturbations of double its spanwise wavelength, may also affect the underlying two-dimensional flow, but since this is already unstable to the eigenmode of figure 10b, computing the second unstable mode is not within the reach of mere time-stepping. Besides, it may also be the case that this second instability is related to the interactions of unstable wavelengths across the continuous eigenspectrum. For $L_z = 5$ the domain admits instability to perturbations of wavelength $\lambda_z = L_z/l$, with $l \in \mathbb{Z}$, or, equivalently, wavenumber $\beta_z = 2\pi/l/L_z$. Now, for $R = 3.4$, the unstable dominant mode can only fit twice or thrice within the domain considered and the system seems to choose $\lambda_z = 2.5$ as the prevailing instability. At $R = 3.8$, instead, the unstable band has grown large enough to allow for the dominant mode to fit either twice, thrice, four times or even just once. The three-dimensional solution has $\lambda_z = L_z = 5$ but it retains a $\lambda_z \simeq 2.5$ -dependence to a large extent. This suggests that the mode with $\lambda_z = 2.5$ and $\lambda_z = 5$, which in fact are one and the same mode except for their different wavelengths, might be competing and that none completely prevails over the other.

Figure 11a shows snapshots of the three-dimensional solution for $R = 3.8$ at four consecutive crossings of the Poincaré section. The original spanwise wavelength $\lambda_z = 2.5$ is preserved to a

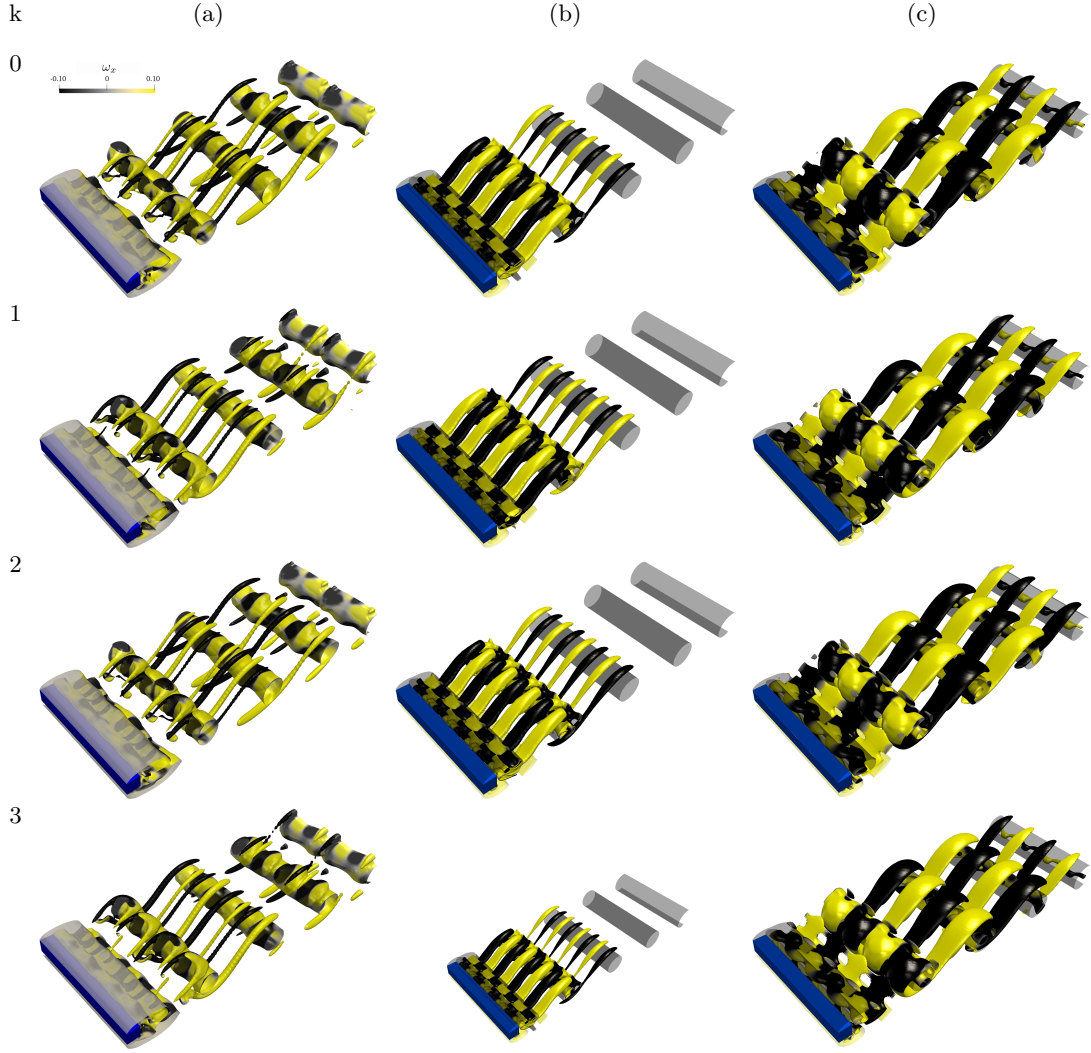


Figure 11: Instantaneous snapshots of (a) the three-dimensional solution at $R = 3.8$ (Movie 3), (b) dominant eigenmode for $(R, \lambda_z) = (3.8, 2.5)$ (Movie 4), and (c) dominant eigenmode for $(R, \lambda_z) = (3.8, 5)$ (Movie 5), at four consecutive crossings of the Poincaré section. Iso-surfaces and colours as for figure 10, except that $Q = 0.0001$ is used to display nonlinear three-dimensional vortical structures.

large extent, but the actual periodicity is now the full $\lambda_z = L_z = 5$. The similarity with $R = 3.4$ is apparent, but the elongated vortices along the braids reach further downstream into the wake. Although crossings 0 and 2 (also 1 and 3) look very much alike, careful inspection reveals that very slight differences exist that are related with the period-doubled nature of the solution. Also hard to notice, but nevertheless present, is the symmetry that leaves the solution invariant after evolution over two consecutive crossings of the Poincaré section followed by reflection about appropriately chosen streamwise-cross-stream planes.

The spanwise periodicity $\lambda_z = 5$ is doubtless unrelated to a mode A instability despite the compatible wavelength. The typical features of mode A are absent from the wake, while mode C vortical structures clearly prevail, albeit with a two-fold subharmonic spanwise modulation. In order to discard any involvement of mode A in the solution observed at $R = 3.8$, 4 consecutive normalised snapshots of the dominant mode for wavelengths $\lambda_z = 2.5$ and 5, both unstable according to figure 3, are shown in figures 11b and c, respectively. The spatial structure of the dominant eigenmode is clearly the same at both wavelengths, with minor differences that are perfectly imputable to a continuous transformation from one to the other. Moreover, the two modes are definitely of the C type, that is subharmonic, as normalised snapshots taken exactly two vortex-shedding cycles apart

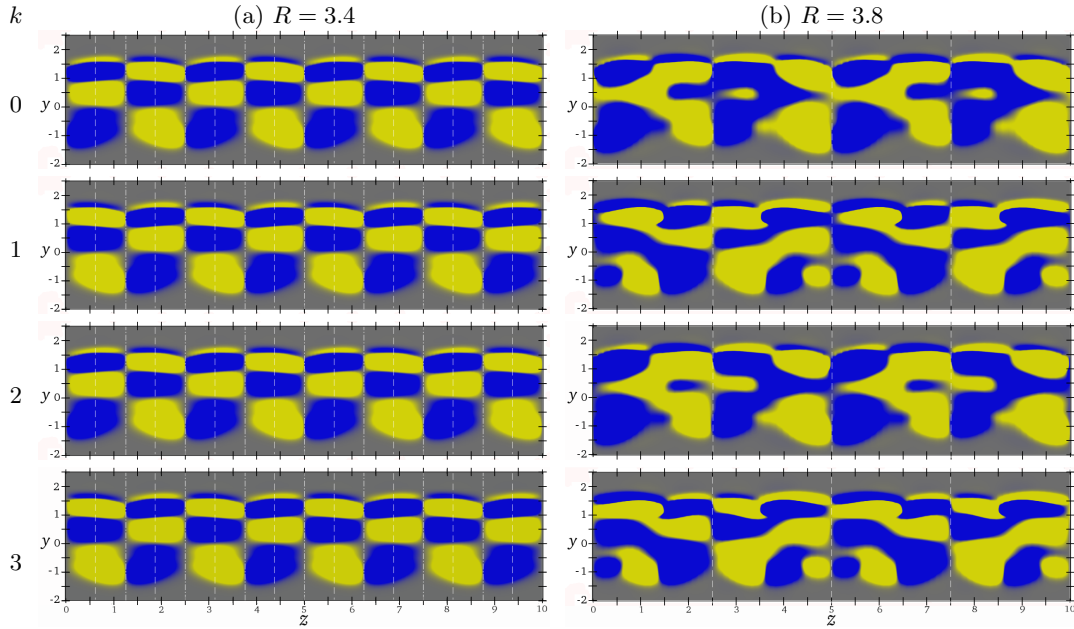


Figure 12: Streamwise vorticity colourmaps $\omega_x \in [-0.1, 0.1]$ (yellow for positive, black for negative) at $x = 6$ for velocity ratios (a) $R = 3.4$ and (b) $R = 3.8$. Four consecutive crossings of the Poincaré section have been represented, respectively.

are identical in all respects, and those taken only one vortex-shedding cycle apart are related by the space-time symmetries described earlier. Therefore, the actual frequency and symmetry-breaking of the nonlinear solution at $R = 3.8$ cannot be explained by a period-doubling bifurcation affecting also the already unstable two-dimensional vortex-shedding solution. The origin of the period-doubling must probably be sought in some modulational instability of the nonlinear solution at $R = 3.4$.

Colourmaps of streamwise vorticity ω_x on a spanwise-cross-stream plane located at $x = 6$ in the cylinder wake -the precise location of the Kármán vortex centre at the instants chosen for the snapshots- help pinpoint the actual spanwise wavelength and space-time symmetry of the three-dimensional solutions for $R = 3.4$ and $R = 3.8$ in figures 12a and b, respectively. The exact repetition of the solution every two crossings of the Poincaré section is now evinced by the exact matching of crossings 0-2 and 1-3 for $R = 3.4$. The symmetry planes at $z = z_0 + (2j)\lambda_z/4 = 2.5j$ are perfectly identifiable, as is also clear that even/odd Poincaré crossings are mutually related by a reflection about planes at $z = z_0 + (2*j+1)\lambda_z/4 = 1.25 + 2.5j$. Note that reflection symmetries, as is the case of the two symmetries discussed here, imply a change of sign of ω_x , hence the change of colour. Both symmetries combined result in a third symmetry that is detectable as a shift by $\lambda_z/2 = 1.25$ from one Poincaré crossing to the next.

For $R = 3.8$, the planes $z = z_0 + (2j)\lambda_z/4 = 2.5j$ are no longer symmetry planes, although the solution keeps the shadow of a reflectional symmetry to a certain extent. Remnants of the original spanwise periodicity $\lambda_z = 2.5$ are also still perceptible, but the actual periodicity has indeed doubled to $\lambda_z = 5$. The only remaining symmetry, which is of a spatio-temporal nature, relates even/odd crossings by a reflection about planes at $z = z_0 + (2j)\lambda_z/4 = 2.5j$.

A single snapshot of a random crossing of the Poincaré section for the chaotic solution at $R = 5.357$ is shown in figure 13a. The Kármán vortices are still clearly identifiable as are also the elongated vortical structures along the braids, which are clearly arranged in pairs forming horse-shoe vortices on top of the primary spanwise vortices. The flow remains fairly well organised in the near wake, but clearly breaks into turbulent dynamics a little further downstream. The typical wavelength of the vortical structures remains of about $\lambda_z \sim 2.5$, but there is no spanwise periodicity other than that artificially imposed by the fundamental Fourier mode employed in the simulation, here $L_z = 10$. A second emerging sub-dominant mode of a much shorter spanwise wavelength, already visible at the far end of the Floquet spectrum of figure 3, is shown in figure 13b. The mode is still stable at $R = 5.357$, but bifurcates with critical $\lambda_z \simeq 10/7$ for $R < 6.5$. Its characteristically

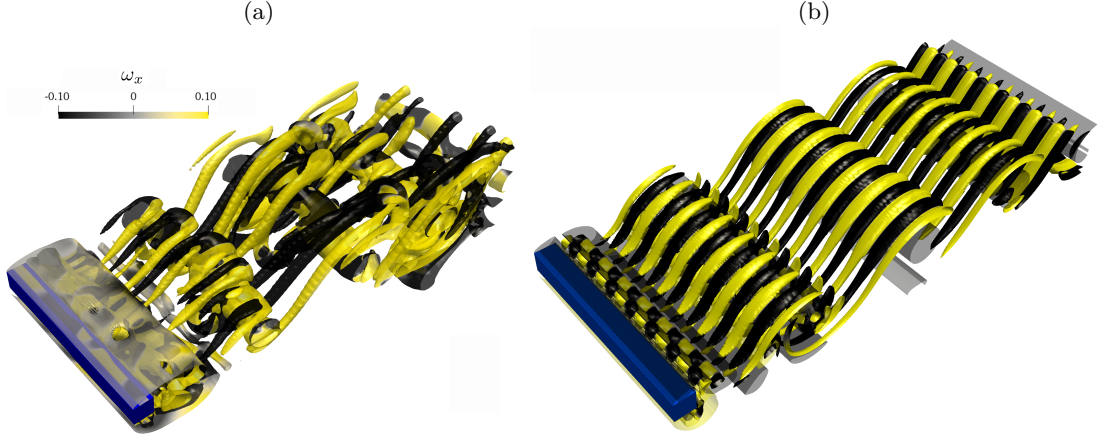


Figure 13: Instantaneous snapshot of (a) the chaotic three-dimensional solution at $R = 5.357$ at a random crossing of the Poincaré section, and (b) short wavelength dominant eigenmode at $(R, \lambda_z) = (5.357, 1.429)$. Iso-surfaces and colours as for figure 11.

short wavelength and synchronous nature identify it as mode-B type. It is however not detectable in the turbulent snapshot and its growth rate once unstable remains well below that of the dominant eigenmode for $\lambda_z \simeq 2.5$, which in fact has shifted to even larger values for these high values of R . It is therefore improbable that this other mode plays any important role in the transition to turbulence of the wake past the square cylinder in upstream shear.

A quasi-static variation of R , which is out of the scope of this study, would be required to cast light on the actual path leading to turbulence, but the presence of a period-doubling bifurcation suggests that a period-doubling cascade might play a role. There is also evidence suggesting that the complexification of the dynamics might arise from the competition of an increasing number of unstable wavelengths of the same instability type (actually a continuum if an infinite-span cylinder was to be considered), so that an instability of the Eckhaus or Benjamin-Feir type might in fact be held responsible, both for the period-doubling bifurcation reported here and the route to chaotic dynamics (Lewke *et al.* 1993; Lewke & Provansal 1994, 1995).

Although the dominant eigenmode curves in the Floquet spectrum of figure 3 are smooth in the range of wavelengths observed in nonlinear solutions, evidence that they represent the same actual instability requires a close inspection of the eigenfields. Four snapshots taken at consecutive crossings within the linear regime of a purposefully designed Poincaré section, well before three-dimensional modal energy reaches nonlinear saturation, illustrate the flow topology of the instability for $(R, \lambda_z) = (3.4, 2.5)$, $(3.8, 2.5)$ and $(3.8, 5)$ in figure 14. Shown are normalised streamwise vorticity ω_x colourmaps on a streamwise-cross-stream plane halfway between two consecutive symmetry planes of the eigenmode. Comparison of all three cases points at a common origin of all three instabilities, which in fact are one and the same mode just deformed by a continuous change of the parameters. The only apparent effect, besides the stretching/compressing associated to changes in λ_z which was already obvious from figures 11b and c, is that the instability dissipates faster along the wake when R is increased or the wavelength shortened towards criticality.

The instability grows preferentially in the very near wake, where the perturbation $|\omega_x|$ is maximum, and the period-doubling nature of the mode is obvious from the coincident normalised ω_x fields of any two snapshots taken exactly two vortex-shedding cycles apart. The appropriate choice of the spanwise plane used for the representation also substantiates the evident fulfilment of a space-time symmetry through a mere change of sign of ω_x between any two consecutive Poincaré crossings. The topology and symmetries of the eigenmode consummately foreshadow the properties of the nonlinear three-dimensional solution observed for $R = 3.4$ and act as harbingers of the main features of the flow arrangement for $R = 3.8$, but cannot by themselves explain the actual spanwise periodicity or the period-doubled nature of the latter. We surmise that the $\lambda_z = 5$ instance of the eigenmode might be interfering with the dominant $\lambda_z = 2.5$ eigenmode at $R = 3.8$, such that the nondimensional features arise from an Eckhaus- or Benjamin-Feir-type instability. Simulations in much longer spanwise domains would be required to sufficiently approximate the continuous band

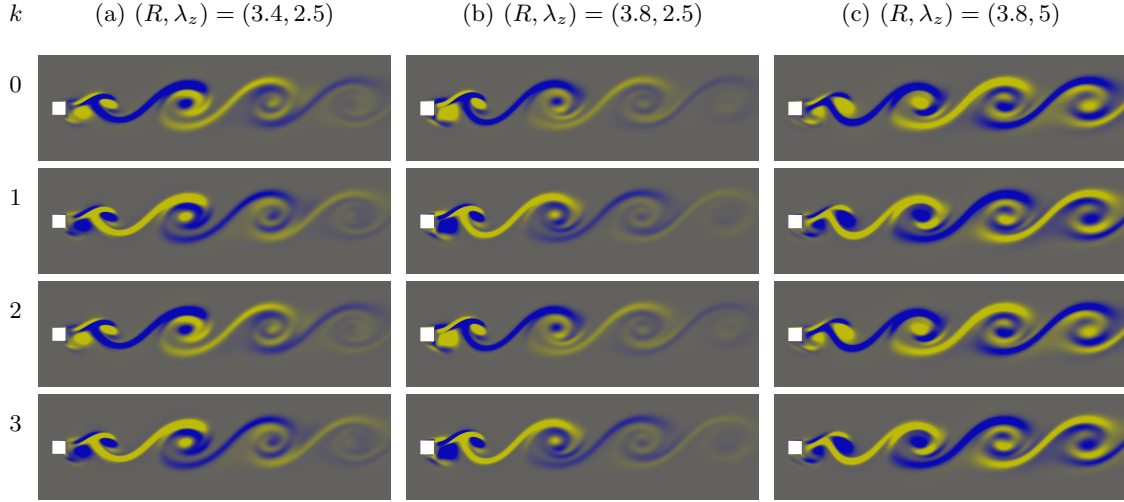


Figure 14: Most unstable mode for $Re_B = 56$ and (a) $(R, \lambda_z) = (3.4, 2.5)$ (Movie 6), (b) $(R, \lambda_z) = (3.8, 2.5)$ (Movie 7), and (c) $(R, \lambda_z) = (3.8, 5)$ (Movie 8). Normalised streamwise vorticity ($\omega_x \in [-1, 1]$) colourmaps at plane $z = z_0 + \lambda_z/4$ at four consecutive Poincaré crossings (marked and labeled in figure 3a for case (a)).

of unstable wavelengths that would be required to allow for mode competition and thus analyse the bifurcation in the light of modulational instabilities.

7. Conclusions

We have investigated the incompressible Newtonian flow past an infinite square cylinder immersed in the wake of an upstream flat plate separating two streams of different velocities. The cylinder is therefore subject to an incoming shear flow consisting of a (nearly) step velocity profile instead of the more classic case of homogeneous shear, which presents serious limitations in its realisation both experimentally and numerically, particularly so when three-dimensionality is to be expected and Couette flow has become prone to subcritical transition. The splitter plate length and upstream distance from the cylinder being fixed, the problem is governed by two parameters, namely the bulk Reynolds number Re and the velocity ratio R . Here we have chosen to keep the bottom stream Reynolds number $Re_T = 56$ fixed and vary only R , such that the closely related shear parameter $K \equiv 2(R-1)/(R+1)$ and $Re \equiv (R+1)Re_B/2 = 28(R+1)$ are linked.

Several aerodynamic performance parameters have been assessed along the path from the steady symmetric solution towards the highly asymmetric and spatio-temporally chaotic wake dynamics. Pressure forces, particularly on the upper half of the front wall, have been shown to be the main contributor to the drag coefficient C_d , which increases with R , particularly after the onset of vortex shedding. The lift coefficient C_l is dominated by downward friction on the front wall at low values of R , thus producing a net downforce. Time-dependence sets the pressure difference between top and bottom on an increasingly growing trend that ends up yielding positive lift. Force coefficient fluctuations C'_l and C'_d increase while the solution remains two-dimensional but stagnate to rather constant values once three-dimensionality sets in. The Strouhal number St is rather stable, with a slightly increasing trend mainly pulled by the increase in Re , while the independent effect of K is unknown but probably decreasing.

Much of the behaviour exhibited by the flow configuration analysed here bears compelling analogy to the somewhat related case of bluff bodies immersed in homogeneous upstream shear. It is therefore probable that the velocity jump across the bluff body cross-stream length-scale is in fact to be held responsible for most of the observed phenomena, the actual shape of the velocity profile (linear or step-like) playing only a subsidiary role.

The symmetric case $R = 1$ ($Re = 56$, $K = 0$) is steady, implying that the presence of the splitter plate has a stabilising effect, through the viscous blockage effect, on the flow past a square cylinder, which is known to undergo a Hopf bifurcation somewhat earlier at $Re^H \simeq 45$. The first bifurcation

upon increasing R remains the two-dimensional onset of time-periodicity, but this only happens for $R = 2.1 \pm 1$ ($Re = 86.8 \pm 2.8$, $K = 0.71 \pm 0.04$). It cannot be concluded from present results whether the delay in the onset of time-dynamics is due to the presence of the splitter plate or whether the upstream velocity ratio also has a stabilising effect.

Once vortex-shedding is in place, the Kármán vortex street in the cylinder wake follows the same trends observed in the literature. The vortices on the high velocity side become stronger and rounder with shear, while those on the low velocity side are weak, elongated and dissipate fast in the wake.

Stability analysis of the time-periodic two-dimensional vortex-shedding solution to three-dimensional perturbations reveals three distinct modes. A long wavelength mode, possibly related to the mode A that is ubiquitous in the wake transition regime of the classic circular and square cylinders, is dominant but stable for velocity ratios $R \leq 3$. At the high R end, a very short wavelength mode arises and bifurcates for $R \gtrsim 6$, but is never even close to dominant. The last mode, of an intermediate wavelength, prevails for $R > 3$ and is the one responsible for wake three-dimensionalisation along the increasing R path followed here. This mode bifurcates at $R^C \simeq 3.1$ ($Re^C \simeq 115$, $K^C \simeq 1.02$) with critical wavelength $\lambda_z^C \simeq 2.4$, exhibits elongated streamwise-cross-stream vortical structures along the braids connecting consecutive clockwise Kármán vortices, and is subharmonic (period-doubling). While breaking the spanwise translational invariance $SO(2)$ of the two-dimensional time-periodic solution, which belongs to the $O(2)=Z_2 \times SO(2)$ symmetry group class, it still preserves a collection of symmetries. Besides repeating every two vortex-shedding cycles, the eigenfields are mirror symmetric with respect to a discrete number of spanwise planes every $\lambda_z/2$, and also invariant under the evolution by half a period (one vortex-shedding cycle) followed by either reflection about spanwise planes located halfway between contiguous reflection-symmetry planes or shift by half a wavelength $\lambda_z/2$. The wavelength, topology and symmetries of the mode are typical of the mode C that is characteristic of the wake transition regime of open rings or square cylinders at incidence, and known to evolve from the quasiperiodic mode QP previously reported for circular and square cylinders. Converged three-dimensional nonlinear solutions slightly beyond the bifurcation point exhibit time dynamics and wake structures sharing all properties that are characteristic of mode C.

At somewhat higher $R \in (3.4, 3.8)$, the flow undergoes a tertiary bifurcation that doubles the period yet again (nonlinear solutions repeat every 4 vortex-shedding cycles) and also doubles the spanwise wavelength. The instability is therefore of the modulational type and amplifies perturbations that have double the wavelength of the original spanwise-periodic pattern. The resulting nonlinear solution has been observed in a computational domain with $L_z = 5$, allowing only for a discrete number of periodic patterns with wavelengths $\lambda_z = L_z/j = \{5, 2.5, 1.667, 1.25, \dots\}$. The spanwise mirror symmetry has finally been broken and the only remaining invariance besides the four-fold time-periodicity is a space-time symmetry that recovers the solution by applying a reflection after the evolution by half a period (two vortex-shedding cycles). There is no evidence of a secondary bifurcation of the two-dimensional solution exhibiting a $\lambda_z = 5$ other than a stretched version of the same mode C, which has also become unstable. As a matter of fact, the range of unstable wavelengths for which mode C is unstable increases with R but the dominant wavelength remains quite fixed at $\lambda_z \simeq 2.5$ for $R \leq 4$ and only migrates to increasingly wider values beyond this point. It is probable that the observed period-doubling bifurcation must be understood in the light of an Eckhaus instability, whereby a periodic pattern becomes modulationally unstable following the bifurcation of a widening spectrum of competing wavelengths.

Very shortly after the period-doubled three-dimensional pattern, a further increase in R brings spatio-temporal chaos with it. Simulations in much longer domains, allowing for a larger set of unstable wavelengths, would be required in the wake transition regime so as to elucidate the actual nature of the route to chaotic dynamics and turbulence, but this is beyond the scope of the present investigation.

8. Acknowledgements

This work was supported by the Spanish Government grants FIS2016-77849-R and PID2020-114043GB-I00, and by the Catalan Government grant 2017-SGR-00785, respectively. Part of the

	d_w	A_c	N_{xy}	St	[%]	$\langle C_d \rangle$	[%]	C'_l	[%]
Mesh A	1.0×10^{-2}	1.0×10^{-4}	84678	0.162	[+1.25]	1.543	[+3.10]	0.302	[+5.59]
Mesh B	2.4×10^{-3}	2.4×10^{-5}	95294	0.160	[+0.00]	1.500	[+0.33]	0.291	[+1.57]
Mesh C	1.2×10^{-3}	1.2×10^{-5}	125204	0.160		1.495		0.286	
Wang et al. (2016) [Case 1]		1.7×10^{-4}		0.160		1.474		0.285	
Ali et al. (2009) [Case E]	1.0×10^{-2}	1.0×10^{-4}	228800	0.160		1.470		0.285	
Doolan (2009)				0.156		1.440		0.293	
Franke et al. (1990)	3.8×10^{-3}		6688	0.165		1.560			

Table 1: Resolution study for the two-dimensional flow past a stand-alone square cylinder at $Re = 150$. d_w denotes the maximum thickness of wall-adjacent elements, A_c is the minimum cell area, and N_{xy} is the total cell count. Reported are the vortex-shedding non-dimensional frequency St , the mean drag coefficient $\langle C_d \rangle$ and the rms of the lift coefficient C'_l , alongside the relative error with respect to mesh C results in brackets.

computations were done in the Red Española de Supercomputación (RES), the Spanish supercomputer network, under grants FI-2019-1-0023 and FI-2018-3-0030.

Appendix A. Resolution study

The time-stepping scheme and space discretisation used here for the flow past a square cylinder immersed in the wake of an upstream splitter plate separating two streams with different velocities have been validated against literature results using as benchmark the closely related problem of the flow past a stand-alone square cylinder in homogeneous flow at zero angle of attack and at comparable Reynolds numbers.

In the present study, the bottom stream Reynolds number has been kept fixed to $Re_B = 56$ throughout, while the top-to-bottom velocity ratio has been varied in the range $R \in [1, 5.357]$. The corresponding top stream Reynolds number is then $Re_T = RRe_B \leq 300$, and it makes therefore sense to use benchmark results for the classical square-cylinder-flow configuration at $Re = 300$ for mesh validation. The flow remains nevertheless two-dimensional for $R \lesssim 3.1$, so that the in-plane mesh for two-dimensional simulations might be safely based on comparison against square cylinder results anywhere beyond $Re \geq 115$.

The stand-alone square cylinder at $Re = 150$, just short of entering the wake transition regime, has been selected as the benchmark for the design of the in-plane two-dimensional mesh for all two-dimensional cases. Three different levels of refinement have been tested as shown in table 1.

In-plane cell counts of $N_{xy} = 84678$ (Mesh A), 95294 (Mesh B) and 125204 (Mesh C) have been deployed, with maximum thickness of wall elements $d_w = 10^{-2}$, 2.4×10^{-3} and 1.2×10^{-3} , respectively, and minimum cell areas of $A_c = 10^{-4}$, 2.4×10^{-5} and 1.2×10^{-5} . The vortex-shedding frequency (Strouhal number St) compares favourably with literature results, particularly so with the well-resolved computations of case 1 by Wang et al. (2016) and case E by Ali et al. (2009). The same goes for the r.m.s. of the lift coefficient C'_l . The mean drag coefficient $\langle C_d \rangle$ is a little off by about 1.5%, still within acceptable deviation. Furthermore, while the coarsest mesh A produces still considerable error with respect to the finest Mesh C, the intermediate Mesh B falls within 1.5% accuracy for all three monitored parameters. The maximum wall distance of the first layer of cells, measured in wall units ($y^+ \equiv yu_\tau/\nu$, with $u_\tau \equiv \sqrt{\tau_w/\rho}$ the friction velocity) resulted in 1.4, 0.3 and 0.14 for meshes A, B and C, respectively, always well inside the viscous sublayer of the boundary layer. In combination with a very slow progression of cell thickness away from the wall, this is a good indication that boundary layers are well resolved. Accordingly, Mesh B has been taken as sufficiently accurate for two-dimensional simulations with $R \leq 3.1$.

Mesh B has been selected also as the base for three-dimensional simulations at $R > 3.1$ and two different three-dimensional resolutions have been tested for the stand-alone cylinder at $Re = 200$. Results and comparison with published data are summarised in table 2. The three-dimensional meshes result from the extrusion of the in-plane mesh in the spanwise direction, this coordinate

	L_z	L_x^u	L_x^d	H	N_z	N_{xy}	$N(\times 10^6)$	St	C_l'	$\langle C_d \rangle$
Mesh B ₁	18	9	25.5	16	32	95294	3.05	0.156	0.298	1.497
Mesh B ₂	9	9	25.5	16	32	95294	3.05	0.154	0.285	1.493
Mahir (2017)	6	7.5	19.5	15	25	22479	0.56	0.154	—	1.518
Luo et al. (2007)	—	—	—	—	—	—	—	0.160	—	—
Saha et al. (2003)	6	6	17.5	10	22	14240	0.31	0.166	—	1.590
Luo et al. (2003)	—	—	—	—	—	—	—	0.159	—	—
Sohankar et al. (1999)	6	D	12.5	18	25	20449	0.51	0.157	—	1.390
Okajima et al. (1990)	—	—	—	—	—	—	—	0.136-0.154	—	—
Okajima (1982)	—	—	—	—	—	—	—	0.139-0.145	—	—

Table 2: Mesh assessment for three-dimensional computations at $Re = 200$.

	L_z	L_z^u	L_z^d	H	N_z	N_{xy}	$N(\times 10^6)$	St	C_l'	$\langle C_d \rangle$
Mesh B ₃	2	9	25.5	16	32	95294	3.04	0.125	1.529	2.240
Mesh C ₁	2	9	25.5	16	32	125204	4.01	0.123	1.562	2.225
Mesh C ₂	2	9	25.5	16	50	125204	6.26	0.120	1.603	2.214
Mesh C ₃	4	9	25.5	16	100	125204	12.52	0.119	1.609	2.212
Bai & Alam (2018) LES	4	8	16	16	48	62000	2.98	0.125	—	2.210
Norberg (1993)	—	—	—	—	—	—	—	0.127	—	2.227
Okajima et al. (1990)	—	—	—	—	—	—	—	0.118:0.136	—	—
Davis et al. (1984)	—	—	—	—	—	—	—	0.137	—	2.046
Okajima (1982)	—	—	—	—	—	—	—	0.119:0.123	—	—

Table 3: Three-dimensional mesh assessment at $Re = 1000$ for the flow past a square cylinder in homogeneous upstream flow.

being discretised using Fourier spectral expansions of order $N_z = 32$ over a periodic length $L_z = 18$ and 9 for meshes B₁ and B₂, respectively. Agreement with published results is fair in both cases.

As in the present study some of the simulations are performed at a velocity ratio of $R = 5.357$, corresponding to a top Reynolds numbers about $Re_T = 300$, the appropriate mesh must be able to capture spatio-temporal chaos at sufficiently large values of Re .

A final grid refinement study has been undertaken at $Re = 1000$ and the results listed in table 3.

In-plane meshes B and C have been extruded in the spanwise direction to $L_z = 2$ and 4, and the spanwise resolution increased to $N_z = 50$ and 100 for the C mesh. Results using in-plane mesh C are in very good agreement with literature results, although mesh B also yields fairly acceptable errors.

In the present paper, the spanwise extent of the domain for three-dimensional simulations has been adjusted to fit an integer number of times (commonly 2) the most unstable wavelength as obtained from stability analysis of the two-dimensional time-periodic underlying solution. The spanwise resolution has been chosen in each case to ensure a modal energy decay of about 6 orders of magnitude from the largest non-zero spanwise mode. An example is provided by the modal energy evolution for the converged solution at $R = 3.8$ shown in figure 1. The decay from spanwise mode 1 to the last mode 16 is good enough to claim sufficient spanwise resolution.

Appendix B. Stability analysis of periodic solutions

The spanwise translational invariance of the two-dimensional vortex-shedding flow past an infinite square cylinder breaks as the Reynolds number is increased beyond a critical threshold. Floquet theory provides the framework for analysing the stability of time-periodic base flows and has been employed successfully to shed light on the three-dimensionalisation of the wake behind

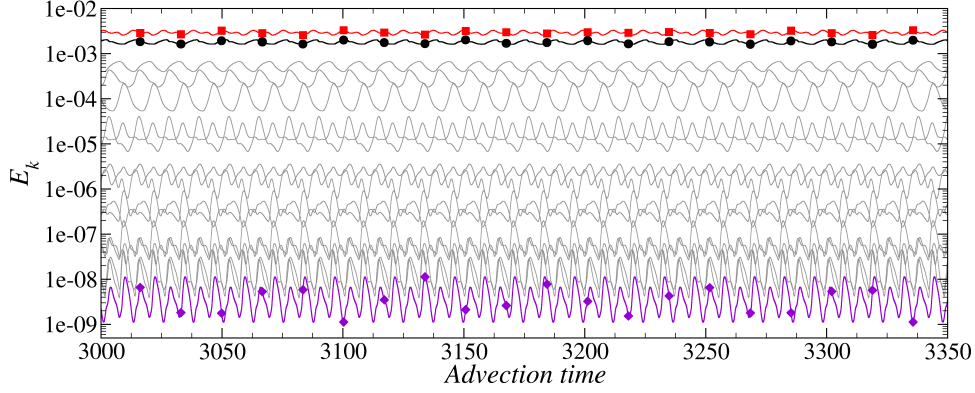


Figure 1: Time evolution of the modal energies E_k contained in the 16 spanwise-dependent modes of the converged solution at $R = 3.8$ in a domain $L_z = 5$. Shown in colour are the spanwise wavenumbers 1 (black line), 2 (red line), and 16 (violet line).

cylinders (Noack & Eckelmann 1994; Henderson & Barkley 1996; Barkley & Henderson 1996). The instantaneous flow is decomposed into the additive superposition of the periodic solution and a perturbation following

$$(\mathbf{u}, p) = (\mathbf{U}, P) + (\tilde{\mathbf{u}}, \tilde{p}). \quad (\text{B } 1)$$

Formal substitution into the Navier-Stokes equations (2.1) and linearisation yields the governing equations for the perturbation field

$$\begin{aligned} \frac{\partial \tilde{\mathbf{u}}}{\partial t} + (\tilde{\mathbf{u}} \cdot \nabla) \mathbf{U} + (\mathbf{U} \cdot \nabla) \tilde{\mathbf{u}} &= -\nabla \tilde{p} + \frac{1}{Re} \nabla^2 \tilde{\mathbf{u}} \\ \nabla \cdot \tilde{\mathbf{u}} &= 0, \end{aligned} \quad (\text{B } 2)$$

with homogeneous conditions on all boundaries of the same typology as for the nonlinear problem.

The two-dimensionality of the base flow and the translational invariance in the spanwise direction allow for the following modal ansatz:

$$\tilde{\mathbf{u}}(\mathbf{r}; t) = \int_{-\infty}^{\infty} \hat{\mathbf{u}}(x, y, \beta; t) e^{i\beta_z z} d\beta_z, \quad (\text{B } 3)$$

corresponding to a Fourier decomposition, such that spanwise modes $\hat{\mathbf{u}}(x, y, \beta; t)$ of different spanwise wavenumber β_z decouple exactly.

Since we are not interested in computing the full eigenspectrum nor even a subset of it, we follow here a simple time-stepping approach that provides the most unstable (or least stable) multiplier for any desired Reynolds number Re and spanwise wavenumber β_z . We perturb the two-dimensional periodic vortex-shedding solution, duly computed through time stepping in the two-dimensional domain where it remains stable, with a tiny spanwise-dependent random disturbance. The initial condition thus obtained is then evolved in time integrating the full nonlinear Navier-Stokes equations but using a single spanwise Fourier component, besides the homogenous component, in a domain of spanwise size $L_z = 2\pi/\beta_z$. After the initial transients, the energy contents on the stable manifold vanish and the perturbation aligns with the dominant eigenmode. At this stage, the dominant eigenmode can be extracted directly from the only non-homogeneous Fourier component of the simulation as long as it does not approach zero-machine (in the stable case) or saturation unto the nonlinear regime (for the unstable case), where it starts feeding energy back into the homogeneous Fourier component via the nonlinear advection term and the simulation becomes utterly under-resolved.

While still in the linear regime, but well past the initial transients, the already modal perturbation follows an oscillating behaviour with the periodicity of the underlying two-dimensional solution on top of an exponential decay/growth. The decay/growth rate of the dominant Floquet mode (as represented by the Floquet multiplier μ) can be derived from the energy time-series of the β_z -mode by fitting a power-law to the sequence of crossings ($E_{\beta_z}^k = E_{\beta_z}(t_k)$) of a purposely defined Poincaré section (in our case, picking $C_l = 0$, and numbering the consecutive crossings at times t_k by an

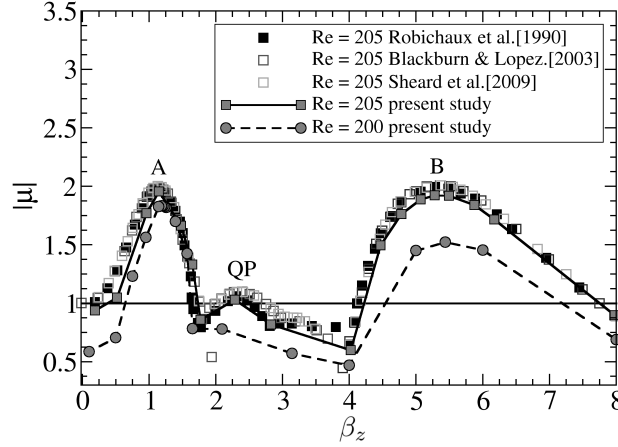


Figure 2: Dominant Floquet multipliers at Reynolds numbers $Re = 200$ (circles) and $Re = 205$ (squares) for the square cylinder without splitter plate. Shown are our numerical results (grey) alongside those by Robichaux *et al.* (1999) (black). Labels indicate modes A, B and QP.

index k)

$$E_{\beta_z}^k = E_{\beta_z}^0 |\mu|^{2k}. \quad (\text{B } 4)$$

Here $E_{\beta_z}^0$ is an irrelevant fitting parameter, while the 2 in the exponent deals with the square relation that exists between the velocity field and its corresponding kinetic energy. A more sophisticated fit of the form

$$a_{\beta_z}^k = a_{\beta_z}^0 r^k \cos(k\theta + \psi), \quad (\text{B } 5)$$

where a is any primitive degree of freedom of the perturbation field (a point velocity component, for example), ψ is another fitting parameter representing an initial phase and $\mu \equiv re^{\pm i\theta}$ a complex multiplier, allows discrimination between synchronous and quasiperiodic modes (An *et al.* 2019). We have not used such a fit here, as the only mode present is clearly subharmonic and appears as synchronous when inspecting the modal energy evolution.

The envelope of the spectrum $|\mu|(\beta)$ for $Re = 200$ and 205 has been computed as proof of concept of the aforementioned method, and compared to published results (Robichaux *et al.* 1999; Blackburn & Lopez 2003; Sheard *et al.* 2009) in figure 2. The agreement is fair at $Re = 205$, for which all three modes, A, B and QP, are duly observed and exhibit the right growth rate dependence on the wavenumber. The most unstable modes at $Re = 200$ have wavenumbers $\beta_z^A \simeq 1.21$ (wavelength $\lambda_z^A = 5.2$) and $\beta_z^B \simeq 5.5$ ($\lambda_z^B = 1.15$), in line with experimental (Luo *et al.* 2003) and experimental (Luo *et al.* 2007) results. A third unstable mode arises at $Re^{QP} \simeq 205$ with wavenumber $\beta_z^{QP} \simeq 2.2$ ($\lambda_z^B \simeq 2.8$), that was not clearly discernible at $Re = 200$. This mode, which was initially thought subharmonic and called mode S (Robichaux *et al.* 1999), is in fact quasiperiodic (Blackburn & Lopez 2003; Sheard *et al.* 2009), hence the name QP, and has already been detected, albeit at much higher Re , for the flow past circular cylinders (Barkley & Henderson 1996; Blackburn & Lopez 2003).

In the light of these results, non-linear three-dimensional simulations at these values of the Reynolds number would need to fit several times the longest mode (A) so that a decent range of the known unstable linear modes are allowed to play their part in selecting/driving the fully non-linear solution.

REFERENCES

- ALI, M.S.M., DOOLAN, C.J. & WHEATLEY, V. 2009 Grid convergence study for a two-dimensional simulation of flow around a square cylinder at a low Reynolds number. In *Seventh International Conference on CFD in The Minerals and Process Industries* (ed. P.J Witt & M.P Schwarz), pp. 1–6.
- AN, BO, BERGADA, J.M. & MELLIBOVSKY, F. 2019 The lid-driven right-angled isosceles triangular cavity flow. *J. Fluid Mech.* **875**, 476–519.
- AN, B., BERGADÀ, J.M., MELLIBOVSKY, F., SANG, W.M. & XI, C. 2020 Numerical investigation on the

- flow around a square cylinder with an upstream splitter plate at low Reynolds numbers. *Meccanica* pp. 1–23.
- AYUKAWA, K., OCHI, J., KAWAHARA, G. & HIRAO, T. 1993 Effects of shear rate on the flow around a square cylinder in a uniform shear flow. *J. Wind Eng. Ind. Aerod.* **50**, 97–106.
- BAI, H. & ALAM, M.M. 2018 Dependence of square cylinder wake on Reynolds number. *Phys. Fluids* **30** (1), 015102.
- BARKLEY, D. & HENDERSON, R.D. 1996 Three-dimensional floquet stability analysis of the wake of a circular cylinder. *J. Fluid Mech.* **322**, 215–241.
- BLACKBURN, H.M. & LOPEZ, J.M. 2003 On three-dimensional quasiperiodic floquet instabilities of two-dimensional bluff body wakes. *Phys. Fluids* **15** (8), L57–L60.
- BLACKBURN, H.M., MARQUES, F. & LOPEZ, J.M. 2005 Symmetry breaking of two-dimensional time-periodic wakes. *J. Fluid Mech.* **522**, 395–411.
- BLACKBURN, H.M. & SHEARD, G.J. 2010 On quasiperiodic and subharmonic Floquet wake instabilities. *Phys. Fluids* **22** (3), 031701.
- CANTWELL, C.D., MOXEY, D., COMERFORD, A., BOLIS, A., ROCCO, G., MENGALDO, G., DE GRAZIA, D., YAKOVLEV, S., LOMBARD, J.E., EKELSCHOT, D. ET AL. 2015 Nektar++: An open-source spectral/hp element framework. *Comput. Phys. Commun.* **192**, 205–219.
- CAO, S., OZONO, S., TAMURA, Y., GE, . & KIKUGAWA, H. 2010 Numerical simulation of Reynolds number effects on velocity shear flow around a circular cylinder. *J. Fluid. Struct.* **26** (5), 685–702.
- CAO, S., ZHOU, Q. & ZHOU, Z. 2014 Velocity shear flow over rectangular cylinders with different side ratios. *Comput. Fluids* **96**, 35–46.
- CHENG, M., WHYTE, D.S. & LOU, J. 2007 Numerical simulation of flow around a square cylinder in uniform-shear flow. *J. Fluid. Struct.* **23** (2), 207–226.
- CHOI, C.B., JANG, Y.J. & YANG, K.S. 2012 Secondary instability in the near-wake past two tandem square cylinders. *Phys. Fluids* **24** (2), 024102.
- DAVIS, R.W. & MOORE, E.F. 1982 A numerical study of vortex shedding from rectangles. *J. Fluid Mech.* **116**, 475–506.
- DAVIS, R., MOORE, E.F. & PURTELL, L.P. 1984 A numerical-experimental study of confined flow around rectangular cylinders. *Phys. Fluids* **27** (1), 46–59.
- DOOLAN, C.J. 2009 Flat-plate interaction with the near wake of a square cylinder. *AIAA J.* **47** (2), 475–479.
- DURAO, D.F.G., HEITOR, M.V. & PEREIRA, J.C.F. 1988 Measurements of turbulent and periodic flows around a square cross-section cylinder. *Exp. Fluids* **6** (5), 298–304.
- FRANKE, R., RODI, W. & SCHÖNUNG, B. 1990 Numerical calculation of laminar vortex-shedding flow past cylinders. *J. Wind Eng. Ind. Aerod.* **35**, 237–257.
- HENDERSON, R.D. & BARKLEY, D. 1996 Secondary instability in the wake of a circular cylinder. *Phys. Fluids* **8** (6), 1683–1685.
- HUNT, J.C.R. 1988 Stream and convergence zones in turbulent flows. *Tech. Rep.*, Center for Turbulence Research.
- HWANG, R.R. & SUE, Y.C. 1997 Numerical simulation of shear effect on vortex shedding behind a square cylinder. *Int. J. Numer. Meth. Fl.* **25** (12), 1409–1420.
- JORDAN, S.K. & FROMM, J.E. 1972 Laminar flow past a circle in a shear flow. *Phys. Fluids* **15** (6), 972–976.
- KANG, S., CHOI, H. & LEE, S. 1999 Laminar flow past a rotating circular cylinder. *Phys. Fluids* **11** (11), 3312–3321.
- VON KÁRMÁN, T. 1911 über den mechanismus des widerstandes, den ein bewegter körper in einer flüssigkeit erfährt. *Nachr. Ges. Wissenschaft. Göttingen math.-phys. Klasse* pp. 509–517.
- VON KÁRMÁN, T. 1912 über den mechanismus des widerstandes, den ein bewegter körper in einer flüssigkeit erfährt. *Nachr. Ges. Wissenschaft. Göttingen math.-phys. Klasse* pp. 547–556.
- KELKAR, K.M. & PATANKAR, S.V. 1992 Numerical prediction of vortex shedding behind a square cylinder. *Int. J. Numer. Meth. Fl.* **14** (3), 327–341.
- KIYA, M., TAMURA, H. & ARIE, M. 1980 Vortex shedding from a circular cylinder in moderate-Reynolds-number shear flow. *J. Fluid Mech.* **101** (4), 721–735.
- KUMAR, A. & RAY, R.K. 2015 Numerical study of shear flow past a square cylinder at Reynolds numbers 100, 200. *Procedia Engineering* **127**, 102–109.
- KWON, T.S., SUNG, H.J. & HYUN, J.M. 1992 Experimental investigation of uniform-shear flow past a circular cylinder. *J. Fluid Eng-T. Asme.* pp. 457–460.
- LANKADASU, A. & VENGADESAN, S. 2008 Onset of vortex shedding in planar shear flow past a square cylinder. *Int. J. Heat Fluid Fl.* **29** (4), 1054–1059.
- LANKADASU, A. & VENGADESAN, S. 2009 Influence of inlet shear on the 3-D flow past a square cylinder at moderate Reynolds number. *J. Fluid. Struct.* **25** (5), 889–896.
- LANKADASU, A. & VENGADESAN, S. 2011 Shear effect on square cylinder wake transition characteristics. *Int. J. Numer. Meth. Fl.* **67** (9), 1115–1134.

- LEI, C., CHENG, L. & KAVANAGH, K. 2000 A finite difference solution of the shear flow over a circular cylinder. *Ocean Eng.* **27** (3), 271–290.
- LEWEKE, T. & PROVANSAL, M. 1994 Model for the transition in bluff body wakes. *Phys. Rev. Lett.* **72** (20), 3174.
- LEWEKE, T. & PROVANSAL, M. 1995 The flow behind rings: bluff body wakes without end effects. *J. Fluid Mech.* **288**, 265–310.
- LEWEKE, T., PROVANSAL, M. & BOYER, L. 1993 Stability of vortex shedding modes in the wake of a ring at low Reynolds numbers. *Phys. Rev. Lett.* **71** (21), 3469.
- LOUCKS, R.B. & WALLACE, J.M. 2012 Velocity and velocity gradient based properties of a turbulent plane mixing layer. *J. Fluid Mech.* **699**, 280.
- LUO, S.C., CHEW, Y.T. & NG, Y.T. 2003 Characteristics of square cylinder wake transition flows. *Phys. Fluids* **15** (9), 2549–2559.
- LUO, S.C., TONG, X.H. & KHOO, B.C. 2007 Transition phenomena in the wake of a square cylinder. *J. Fluid. Struct.* **23** (2), 227–248.
- LYN, D.A., EINAV, S., RODI, W. & PARK, J.H. 1995 A laser-Doppler velocimetry study of ensemble-averaged characteristics of the turbulent near wake of a square cylinder. *J. Fluid Mech.* **304**, 285–319.
- MAHIR, N. 2017 Three dimensional heat transfer from a square cylinder at low Reynolds numbers. *Int. J. Therm. Sci.* **119**, 37–50.
- MANSY, H., YANG, P.M. & WILLIAMS, D.R. 1994 Quantitative measurements of three-dimensional structures in the wake of a circular cylinder. *J. Fluid Mech.* **270**, 277–296.
- MARQUES, F., LOPEZ, J. M. & BLACKBURN, H.M. 2004 Bifurcations in systems with Z2 spatio-temporal and o (2) spatial symmetry. *Physica D* **189** (3–4), 247–276.
- MITTAL, S. & KUMAR, B. 2003 Flow past a rotating cylinder. *JFM* **476**, 303–334.
- MONSON, D.R. 1983 The effect of transverse curvature on the drag and vortex shedding of elongated bluff bodies at low Reynolds number. *J. Fluid Eng.-T. Asme.* pp. 308–318.
- MOSER, R.D. & ROGERS, M.M 1993 The three-dimensional evolution of a plane mixing layer: pairing and transition to turbulence. *J. Fluid Mech.* **247**, 275–320.
- MOXEY, DAVID, CANTWELL, CHRIS D, BAO, YAN, CASSINELLI, ANDREA, CASTIGLIONI, GIACOMO, CHUN, SEHUN, JUDA, EMILIA, KAZEMI, EHSAN, LACKHOVE, KILIAN, MARCON, JULIAN ET AL. 2020 Nek-tar++: Enhancing the capability and application of high-fidelity spectral/hp element methods. *Comput. Phys. Commun.* **249**, 107110.
- MUSHYAM, ADITYA & BERGADA, JOSEP M 2017 A numerical investigation of wake and mixing layer interactions of flow past a square cylinder. *Mec* **52** (1), 107–123.
- NIU, XIAO-FEI, LI, YONG & WANG, XUN-NIAN 2021 Numerical study of aerodynamic noise behaviors for a vertically-installed flat strut behind an asymmetrical airfoil. *European Journal of Mechanics-B/Fluids* **88**, 17–33.
- NOACK, B.R. & ECKELMANN, H. 1994 A global stability analysis of the steady and periodic cylinder wake. *J. Fluid Mech.* **270**, 297–330.
- NORBERG, C. 1993 Flow around rectangular cylinders: pressure forces and wake frequencies. *J. Wind Eng. Ind. Aerod.* **49** (1–3), 187–196.
- NORBERG, C. 1994 An experimental investigation of the flow around a circular cylinder: influence of aspect ratio. *J. Fluid Mech.* **258**, 287–316.
- NORBERG, C. 1996 Taken from Sohankar et al, *Phys. Fluids*, **11**, 288 (1999).
- OKAJIMA, A. 1982 Strouhal numbers of rectangular cylinders. *J. Fluid Mech.* **123**, 379–398.
- OKAJIMA, A., NAGAHISA, T. & ROKUGOH, A. 1990 A numerical analysis of flow around rectangular cylinders. *JSME Int. J. II-Fluid.* **33** (4), 702–711.
- PARK, D. & YANG, K.S. 2016 Flow instabilities in the wake of a rounded square cylinder. *J. Fluid Mech.* **793**, 915–932.
- PARK, D. & YANG, K.-S. 2018 Effects of planar shear on the three-dimensional instability in flow past a circular cylinder. *Phys. Fluids* **30** (3), 034103.
- POSDZIECH, O. & GRUNDMANN, R. 2001 Numerical simulation of the flow around an infinitely long circular cylinder in the transition regime. *Theor. Comput. Fluid Dyn.* **15** (2), 121–141.
- PROVANSAL, M., MATHIS, C. & BOYER, L. 1987 Bénard-von kármán instability: transient and forced regimes. *J. Fluid Mech.* **182**, 1–22.
- RAY, R.K. & KUMAR, A. 2017 Numerical study of shear rate effect on unsteady flow separation from the surface of the square cylinder using structural bifurcation analysis. *Phys. Fluids* **29** (8), 083604.
- ROBICHAUX, J., BALACHANDAR, S. & VANKA, S.P. 1999 Three-dimensional Floquet instability of the wake of square cylinder. *Phys. Fluids* **11** (3), 560–578.
- ROGERS, M.M. & MOSER, R.D. 1992 The three-dimensional evolution of a plane mixing layer: the Kelvin–Helmholtz rollup. *J. Fluid Mech.* **243** (–1), 183.
- SAHA, A.K., BISWAS, G. & MURALIDHAR, K. 1999 Influence of inlet shear on structure of wake behind a square cylinder. *J. Eng. Mech.* **125** (3), 359–363.

- SAHA, A.K., BISWAS, G. & MURALIDHAR, K. 2003 Three-dimensional study of flow past a square cylinder at low Reynolds numbers. *Int. J. Heat Fluid Fl.* **24** (1), 54–66.
- SHEARD, G.J. 2011 Wake stability features behind a square cylinder: focus on small incidence angles. *J. Fluid. Struct.* **27** (5-6), 734–742.
- SHEARD, G.J., FITZGERALD, M.J. & RYAN, K. 2009 Cylinders with square cross-section: wake instabilities with incidence angle variation. *J. Fluid Mech.* **630**, 43–69.
- SHEARD, G.J., HOURIGAN, K. & THOMPSON, M.C. 2005a Computations of the drag coefficients for low-Reynolds-number flow past rings. *J. Fluid Mech.* **526**, 257–275.
- SHEARD, G.J., THOMPSON, M.C. & HOURIGAN, K. 2003 From spheres to circular cylinders: the stability and flow structures of bluff ring wakes. *J. Fluid Mech.* **492**, 147–180.
- SHEARD, GREGORY J, THOMPSON, MARK CHRISTOPHER & HOURIGAN, KERRY 2005b Subharmonic mechanism of the mode C instability. *Phys. Fluids* **17** (11), 111702.
- SOHANKAR, A., NORBERG, C. & DAVIDSON, L. 1998 Low-Reynolds-number flow around a square cylinder at incidence: study of blockage, onset of vortex shedding and outlet boundary condition. *Int. J. Numer. Meth. Fl.* **26** (1), 39–56.
- SOHANKAR, A., NORBERG, C. & DAVIDSON, L. 1999 Simulation of three-dimensional flow around a square cylinder at moderate Reynolds numbers. *Phys. Fluids* **11** (2), 288–306.
- SOHANKAR, A., RANGRAZ, E., KHODADADI, M. & ALAM, M.M. 2020 Fluid flow and heat transfer around single and tandem square cylinders subjected to shear flow. *J. Braz. Soc. Mech. Sci.* **42** (8), 1–22.
- SUNG, H.J., CHUN, C.K. & HYUN, J.M. 1995 Experimental study of uniform-shear flow past a rotating cylinder. *J. Fluid Eng-T. Asme.* pp. 62–67.
- TAMURA, H., KIYA, M. & ARIE, M. 1980 Numerical study on viscous shear flow past a circular cylinder. *Bulletin of JSME* **23** (186), 1952–1958.
- TONG, X.H., LUO, S.C. & KHOO, B.C. 2008 Transition phenomena in the wake of an inclined square cylinder. *J. Fluid. Struct.* **24** (7), 994–1005.
- WANG, J., XU, Y. & CHENG, H. 2016 Features of flow past square cylinder with a perforated plate. *Trans. Tianjin Univ.* **22** (6), 544–554.
- WILLIAMSON, C.H.K. 1988 The existence of two stages in the transition to three-dimensionality of a cylinder wake. *Phys. Fluids* **31** (11), 3165–3168.
- WILLIAMSON, C.H.K. 1992 The natural and forced formation of spot-like vortex dislocations in the transition of a wake. *J. Fluid Mech.* **243**, 393–441.
- WILLIAMSON, C.H.K. 1996a Mode A secondary instability in wake transition. *Phys. Fluids* **8** (6), 1680–1682.
- WILLIAMSON, C.H.K. 1996b Three-dimensional wake transition. *J. Fluid Mech.* **328**, 345–407.
- WILLIAMSON, C.H.K. 1996c Vortex dynamics in the cylinder wake. *Annu. Rev. Fluid Mech.* **28** (1), 477–539.
- YOON, D.H., YANG, K.S. & CHOI, C.B. 2010 Flow past a square cylinder with an angle of incidence. *Phys. Fluids* **22** (4), 043603.
- YOSHINO, F. & HAYASHI, T. 1984 The numerical solution of flow around a rotating circular cylinder in uniform shear flow. *Bulletin of JSME* **27** (231), 1850–1857.
- ZHANG, H.J., HUANG, L & ZHOU, Y 2005 Aerodynamic loading on a cylinder behind an airfoil. *Experiments in fluids* **38** (5), 588–593.